

The influence of polymer concentration and chain architecture on free surface displacement flows of polymeric fluids

Gandharv Bhatara

*Department of Chemical Engineering, Stanford University, Stanford,
California 94305*

Eric S. G. Shaqfeh

*Departments of Chemical and Mechanical Engineering, Stanford University,
Stanford, California 94305*

Bamin Khomami^{a)}

*Materials Research Laboratory, Department of Chemical Engineering, Washington
University, St. Louis, Missouri 63130*

(Received 19 October 2004; final revision received 16 June 2005)

Synopsis

We examine the effect of polymer concentration and chain architecture on the steady state displacement of polymeric fluids by air in between two infinitely long closely spaced parallel plates, i.e., Hele-Shaw flow. A stabilized finite element method coupled with a pseudosolid domain mapping technique is used for carrying out the computations. The constitutive equations employed in this study are the Finitely Extensible Nonlinear Elastic–Chilcott Rallison (FENE-CR) and the Finitely Extensible Nonlinear Elastic–Peterlin (FENE-P) models for dilute solutions, the Giesekus constitutive equation for dilute, semidilute and concentrated solutions, and the Extended Pom-Pom (XPP) constitutive equation for linear and branched polymeric melts. Our study indicates the presence of a recirculation flow at low Ca and a bypass flow at high Ca irrespective of polymer concentration and chain architecture. We show that the interfacial dynamics in both the recirculation and the by-pass flow depend on extensional hardening and shear thinning characteristics of the fluids. In the recirculation flow, we observe the formation of normal elastic stress boundary layers in the capillary transition region, an accompanying increase in the film thickness and a compression of the bubble in the capillary transition region, at moderate Wi . In the bypass flow, in addition to the elastic stress boundary layer in the capillary transition region, an additional stress boundary layer is observed at the tip of the bubble. The amount of film thickening, the magnitude of the stress in the stress boundary layer and the amount of bubble compression are largest for the most extensional hardening fluids and reduce with decreasing extensional hardening and increasing shear thinning. We show that the film thickness is determined by two competing forces, i.e., normal stress gradients in the flow direction, in the capillary transition region (recirculation flow) and the tip region (bypass flow) and shear stress gradients

^{a)} Author to whom correspondence should be addressed; electronic mail: bam@che.wustl.edu; FAX +314 935 7211

in the gap direction. For both the recirculation and the bypass flow, we show how the film thickness scales with fluid normal stresses and shear viscosities, and develop correlations for the film thickness as a function of Ca and Wi . © 2005 The Society of Rheology.
[DOI: 10.1122/1.2000969]

I. INTRODUCTION

The displacement of Newtonian and viscoelastic fluids by air in long narrow tubes plays a central role in many industrial applications such as polymer processing, coating technology, gas-assisted injection molding and enhanced oil recovery [Taylor (1961), Cox (1962), Bretherton (1961), Bonn *et al.* (1995), Ruschak (1985), Coyle *et al.* (1990), Poslinski *et al.* (1995)]. Consequently, numerous researchers have focused their attention on Newtonian displacement flows in a variety of geometries to better understand the interfacial dynamics of free surface flows and prevent free surface instabilities that occur in this class of flows [Pearson (1960), Pitts and Greiller (1961), Sullivan and Middleman (1979), Coyle *et al.* (1990), Rabaud *et al.* (1990)]. However, the number of studies dealing with viscoelastic fluids is very limited [Shaqfeh (1995), Ruschak (1985), Larson (1992)]. To date, most studies have been concerned with film thickness measurements (thickness of the film formed when the fluid is displaced by air) since in most industrial applications, control and uniformity of the film thickness is of primary importance. Hence, our primary focus in this paper will be on examining the influence of polymer concentration and chain architecture on film thickness in a model free surface displacement flow.

In case of Newtonian fluids, the first experimental studies were carried out by Taylor (1961) and Cox (1962) who measured the film thickness as a function of Ca (where Ca is the Capillary number, defined as the ratio of viscous forces to surface tension) obtained when a viscous fluid is displaced out of a tube by an air bubble. The thickness of the film left on the walls by the displaced fluid was observed to increase with increasing Ca . Bretherton (1961) conducted an asymptotic analysis, in addition to experiments, and found good agreement between his asymptotic theory and the experimentally measured film thickness at vanishingly small Ca . Reinelt and Saffman (1985) obtained film thickness results using a finite difference scheme and observed a film thickening effect with increasing Ca . More recently, Park and Homsy (1984) have developed a theory describing two-phase displacement in the gap between closely spaced planes under the assumptions of small Ca and ratio of gap width to transverse characteristic length, and subsequently showed that the film thickness scales as $Ca^{1/3}$.

Turning to the literature on viscoelastic fluids, we find a scarcity of literature in both computational and experimental aspects of the problem. Bonn *et al.* (1995) using solutions of polyethylene oxide (PEO) reported an increase in the film thickness over that found for Newtonian fluids. Linder *et al.* (2002) carried out experiments in a Hele-Shaw cell geometry and observed a film thickness increase over that found for Newtonian fluids using PEO, and a film thickness decrease using xanthane. They attributed the film thickening effect for PEO to the high elongational viscosity and large normal stresses that PEO exhibits, although no clear correlations were developed with Wi . Huzyak *et al.* (1997) reported strong film thickening effects using highly elastic, nonshear thinning, polyisobutene-polybutene (PIB-PB) based Boger fluids. Lee *et al.* (2005) in an experimental study, of a free surface displacement flow of PIB-PB Boger fluids under gravity stabilization in an eccentric cylinder geometry, found significant film thickening due to presence of elasticity. The first theoretical study of a free surface displacement flow of a viscoelastic fluid was carried out by Ro and Homsy (1995). Specifically, the authors formulated a double perturbation expansion in powers of $Ca^{1/3}$ and $Wi/Ca^{1/3}$, (where Wi

is the Weissenberg number, and it provides a measure of the elasticity of the flow through the relaxation time of the polymer) and concluded that for small values of $Wi/Ca^{1/3}$, the fluid elasticity induces resistance to streamwise straining and hence reduces the film thickness. However, this theory is valid for small values of Ca and Wi .

Besides the aforementioned experimental and theoretical contributions, numerical studies have been performed by Pasquali and Scriven (2002), Lee *et al.* (2002), and Bhatara *et al.* (2004), on the steady-state displacement of viscoelastic fluids by an air bubble. Specifically, Pasquali and Scriven (2002) examined the flow dynamics of air displacing fluid for a slot coating flow using dilute and semidilute polymer solutions. They observed the formation of layers of molecular stretch under the free surface downstream of the stagnation point, in the capillary transition region. Furthermore, they showed that the layers of molecular stretch are largest for the extensible and semiextensible molecules and effectively smaller for more rigid molecules. Lee *et al.* (2002), examined both the Hele-Shaw cell geometry and the slot coating geometry for dilute polymer solutions using the Oldroyd-B, FENE-CR and FENE-P constitutive equations. In the Capillary number regime considered in their study (i.e., $Ca < 1.0$), the flow is characterized by a recirculation pattern and the authors show the formation of elastic normal stress boundary layers in the capillary transition region at moderate values of Wi . Furthermore, the authors observed that the formation of these stress boundary layers generates a strong positive normal stress gradient in the flow direction of the capillary transition region that results in film thickening. In addition, it is suggested that the formation of these stress boundary layers is due to the planar extensional nature of the flow near the free surface. Bhatara *et al.* (2004) extended the FENE-CR simulations to a much larger range of Ca and Wi and also incorporated the effect of gravity and channel divergence. They identify the presence of two distinct flow regimes. In the absence of gravity, a recirculation flow at low Ca ($Ca < 1.0$) and a bypass flow at high Ca ($Ca > 1.0$). In the recirculation flow, in addition to the film thickening effect, the authors observe a meniscus invasion phenomenon when the stresses in the boundary layer become very large. In addition, it is also ascertained that the formation of the elastic normal stress boundary layer is mostly a local phenomenon, largely independent of geometrical considerations. Specifically, by increasing the channel divergence the onset of the stress boundary layer and the accompanying film thickening effect is delayed to higher Wi . However, the film thickness normalized with the maximum normal stress in the elastic stress boundary layer collapses onto a single curve.

Motivated by this fact, we have considered the effect of concentration and chain architecture on the flow dynamics of the air displacing fluid flow in a Hele-Shaw cell geometry to ascertain whether the film thickness can be estimated based on specific material properties and the dynamics of the localized stress boundary layers near the free surface. More specifically, we attempt to draw correlations between film thickness and normal stresses in the localized stress boundary layer near the free surface and the rheological characteristics of the fluid model, which in turn indirectly relate to predictions based on concentration and chain architecture effects. To this end, we employ a variety of constitutive equations to model dilute and concentrated polymeric solutions as well as linear and branched polymeric melts. For the dilute solutions we employ the FENE-CR [Chilcott and Rallison (1988)] and FENE-P [Bird *et al.* (1987), Bird *et al.* (1980)] constitutive equations. To model dilute, semi-dilute and concentrated solutions we use the Giesekus constitutive equation [Bird *et al.* (1980), Giesekus (1982)] and for polymeric melts we use the XPP [Verbeeten *et al.* (2001, 2002)] (for both linear and branched polymers) constitutive equation. The choice of the constitutive equations has been made

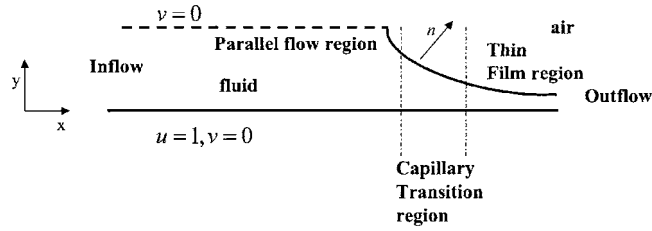


FIG. 1. Schematic of the Hele-Shaw cell flow. The flow domain can be divided into three distinct regions: the thin film region, the capillary transition region, and the parallel flow region.

to satisfy the primary criterion of being able to model the effect of concentration and chain architecture of polymeric fluids, while retaining sufficient mathematical simplicity for computational tractability (i.e., continuum level description).

II. MATHEMATICAL FORMULATION

The governing equations and the solution methodology for the steady free surface problem have been presented in detail in the studies conducted by Lee *et al.* (2002) and Bhatara *et al.* (2004) and we reproduce the equations briefly in this paper.

For the two-dimensional, steady free surface problem depicted in Fig. 1 the governing equations that impose conservation of mass and momentum for an incompressible fluid in this geometry, in the absence of gravity and inertia, are

$$\nabla \cdot \underline{u} = 0, \quad (1)$$

$$-\nabla \frac{P}{Ca} + \nabla \cdot \underline{\tau} = 0, \quad (2)$$

where \underline{u} is the velocity vector, P is the pressure and $\underline{\tau}$ is the total stress tensor formed by the sum of the Newtonian solvent stress, $\underline{\tau}_s$, and the polymer stress, $\underline{\tau}_p$. Ca is the capillary number and is defined as $Ca = \mu U / \sigma$, where μ is the total viscosity of the fluid at zero shear rate, U is the characteristic velocity of the problem, and σ is the surface tension.

The basic equations are nondimensionalized as

$$(x, y) [=] (b, b), \quad (u, v) [=] U, \quad P [=] \frac{\sigma}{b}, \quad \underline{\tau} [=] \frac{\mu U}{b}. \quad (3)$$

A. Dilute polymeric solutions: FENE-CR and FENE-P models

As mentioned before, to model the dynamics of dilute polymeric solutions, we employ elastic dumbbell models, namely, the FENE-CR (for Boger fluids) and FENE-P (to examine the effect of shear thinning) models. Several studies [Lee *et al.* (2002), Pasquali and Scriven (2002), Bhatara *et al.* (2004), Grillet *et al.* (1999)] have previously shown the adequacy of these models to describe the interfacial dynamics of this class of fluids in a variety of simple and complex kinematics flows.

Under steady flow conditions, the constitutive equation for a FENE-CR model is given by

TABLE I. Model parameters used in rheological study and computations.

(a)			
Model	L (extensibility parameter)	S ($\mu_s/\mu_s+\mu_p$)	
FENE-CR	5,10	0.85	
FENE-P	10	0.85	
(b)			
Model	S ($\mu_s/\mu_s+\mu_p$)	α	
Giesekus	0.85	0.01, 0.1	
Giesekus	0.1	0.5	
(c)			
Model	q	λ_b/λ_s	α
XPP	1	7.0	0.5
XPP	5	3.0	0.06

$$\underline{u} \cdot \underline{\nabla} \underline{C} = \underline{C} \cdot \underline{\nabla} \underline{u} + \underline{\nabla} \underline{u}^T \cdot \underline{C} - \frac{f(R)}{Wi} (\underline{C} - \underline{I}), \tag{4}$$

where $Wi=U\lambda/b$ (b is the gap separation between the plates, λ is the relaxation time of the polymeric fluid and U is the mean fluid velocity). \underline{I} is the identity matrix, \underline{C} is the polymer conformation tensor and represents an ensemble average of the dyadic product \underline{RR} of the dumbbell end to end vector \underline{R} . $f(R)$ is the entropic spring force law, given by

$$f(R) = \frac{1}{1 - \frac{Tr(C)}{L^2}}, \tag{5}$$

where L is the finite extensibility parameter, i.e., the ratio of the length of a fully extended polymer to its equilibrium length. The larger the value of L , the more extensible is the polymer. The total stress is written as the sum of the viscous stress and the polymer stress,

$$\underline{\tau} = 2S\dot{\underline{\gamma}} + \frac{(1-S)}{Wi} f(R)(\underline{C} - \underline{I}), \tag{6}$$

where $\dot{\underline{\gamma}}$ is the strain rate tensor, while S is the ratio of the solvent viscosity to the total viscosity and provides a measure of polymer concentration in the fluid. The FENE-P model can be obtained by substituting the term $-f(R)(\underline{C} - \underline{I})/Wi$ by $-[f(R)\underline{C} - \underline{I}]/Wi$.

In this study, the model parameters chosen for both the rheological characterization and the computation for the FENE-CR and FENE-P models are contained in Table I(a). The choice of model parameters is motivated by prior experimental and computational studies with this class of fluids [Lee *et al.* (to be published), Chilcott and Rallison (1988), Bird *et al.* (1987), Oene and Cragg (1962), Noda *et al.* (1968)].

The difference between the two models is that FENE-CR has a constant shear viscosity, while the FENE-P is shear thinning, though the amount of shear thinning depends on the extensibility parameter [i.e., at low shear rates, $\mu - \mu_s \propto L^2/(L^2+3)$ and at high shear rates $\mu - \mu_s \propto L^{2/3}$, where μ is the polymer shear viscosity and μ_s is the solvent viscosity]

[Bird *et al.* (1987)]. In a steady shear flow, i.e., $u=y$, $v=w=0$, at a Wi of 1.0, the FENE-P ($L=10$) model starts to display a slight amount of shear thinning of viscosity while the FENE-CR model remains nonshear thinning. Furthermore, the first normal stress coefficient, Ψ_1 , shear thins for both models, while the second normal stress coefficient, Ψ_2 , is zero [Bird *et al.* (1987)].

In a steady planar extensional flow, i.e., $u=x$, $v=-y$, $w=0$, both models display significant extensional hardening at $Wi=0.5$. Physically, this can be understood as the coil stretch transition that the polymer chains undergo at $Wi=0.5$. Furthermore, it can be observed that the extensional viscosity is bounded as Wi approaches infinity (asymptotes to L^2 for both FENE-CR and FENE-P). In transient planar extensional flow, both FENE-CR ($L=10$) and FENE-CR ($L=5$) display extensional viscosities which increase monotonically with increasing strain, with no stress overshoot, and tending asymptotically towards values corresponding to steady planar extensional flow.

It is worth noting that we are interested in the planar extensional viscometric behavior rather than the uniaxial extensional behavior because the flow (of the air displacing fluid in the Hele-Shaw cell) at the free surface is planar extensional, and we subsequently relate the normal stresses generated at the free surface to the extensional viscosity of the various models.

B. Dilute, semidilute and concentrated solutions: Giesekus model

The Giesekus model (i.e., an elastic dumbbell model with anisotropic hydrodynamic drag on the beads) has been selected for modeling the dynamics of semidilute and concentrated polymeric solutions due to the fact that prior studies have shown that it can adequately describe dynamics of this class of flows in both simple and complex kinematics flows [Giesekus (1982), Burghardt *et al.* (1999)]. Under steady flow conditions the constitutive equation for the Giesekus model can be written as

$$\underline{u} \cdot \underline{\nabla} \underline{C} = \underline{C} \cdot \underline{\nabla} \underline{u} + \underline{\nabla} \underline{u}^T \cdot \underline{C} - \left(\frac{f(R)}{Wi} \underline{C} - \underline{I} \right) + \frac{\alpha}{Wi} (\underline{C} - \underline{I}) [f(R) \underline{C} - \underline{I}]. \quad (7)$$

The parameter α is a model parameter and the term containing α is attributed to anisotropic hydrodynamic drag on the constituent polymer molecules. It should be noted that α can be indirectly related to the concentration of the polymer, i.e., $\alpha=0$ represents dilute solutions, while $\alpha=0.5$ represents concentrated solutions. For physically relevant results it is required that $0 < \alpha < 0.5$, as for values of $\alpha > 0.5$, the shear stress (τ_{xy}) plotted as a function of Wi displays a maximum, which is not observed experimentally for this class of fluids [Bird *et al.* (1987)]. The model parameters chosen for this study are contained in Table I(b).

Under steady shear flow the Giesekus model displays shear thinning. The decrease in the shear viscosity with Wi is enhanced as α is increased. In steady shear flow (i.e., $u=x$, $v=w=0$), for $\alpha > 0$, it can be shown that the shear viscosity asymptotes to $\sqrt{(1-\alpha)/\alpha}$ at high shear rates [Bird *et al.* (1987)]. The first normal stress coefficient decreases with increasing shear rate and the rate of decline increases with increasing α . The second normal stress coefficient is nonzero and negative, and can be varied in magnitude relative to the first normal stress coefficient by adjusting the value of α . Under steady planar extensional flow, for low values of α , extensional hardening (with finite asymptotic value) is observed. The magnitude of the extensional viscosity decreases with increasing α . At $\alpha=0.5$, the Giesekus model displays a very slight extensional hardening behavior and the steady extensional viscosity is largely independent of strain rate. Under transient

planar extensional flow, for all values of (α) , the extensional viscosity shows a monotonic increase with increasing strain and no stress overshoot.

C. Polymeric melts: XPP model

Since theories based on the concept of reptation proposed by deGennes [Doi and Edwards (1986), deGennes (1971)] have emerged as the primary tool for describing the rheology of entangled polymeric systems, we have selected the pom-pom constitutive equation [Verbeeten *et al.* (2001, 2002), Milner and Mcleish (1998)] to investigate the dynamics of polymeric melts. This choice has been motivated by the fact that this model not only contains the essential physics to describe the dynamics of entangled polymeric systems (i.e., evolution equations for the orientation and stretch), but also, by appropriate selection of the model parameters, one can describe the nonlinear rheology of both linear and branched entangled polymeric fluids.

The key feature of the model is the decoupling of relaxation times for stretch and orientation. The simplified topology consists of a chain backbone and a number of dangling arms on both ends of the backbone. Verbeeten *et al.* (2001) incorporated local branch-point displacement and modified the orientation equation of the original differential version to the extended Pom-Pom model in order to resolve three major issues: discontinuities in steady state elongation, unbounded orientation at high strain rates, and a zero second normal stress difference in shear. In addition the XPP model can be written in a differential form that makes it computationally attractive. The constitutive behavior of a single mode XPP model can be represented with the following equations,

$$\underline{u} \cdot \underline{\nabla} \underline{\underline{\tau}} - \underline{\underline{\nabla}} \underline{u}^T \cdot \underline{\underline{\tau}} - \underline{\underline{\tau}} \cdot \underline{\underline{\nabla}} \underline{u} + \lambda(\underline{\underline{\tau}})^{-1} \cdot \underline{\underline{\tau}} = 2G\underline{\underline{D}}, \tag{8}$$

where G is the plateau modulus and $\underline{\underline{D}} = (1/2)(\underline{\underline{\nabla}} \underline{u} + \underline{\underline{\nabla}} \underline{u}^T)$ is the rate of deformation tensor. The function $\lambda(\underline{\underline{\tau}})^{-1}$ is defined as

$$\lambda(\underline{\underline{\tau}})^{-1} = \frac{1}{\lambda_b} \left(\frac{\alpha}{G} \underline{\underline{\tau}} + F(\underline{\underline{\tau}}) \underline{\underline{I}} + G(F(\underline{\underline{\tau}}) - 1) \underline{\underline{\tau}}^{-1} \right), \tag{9}$$

with

$$F(\underline{\underline{\tau}}) = 2r e^{\mu(\Lambda-1)} \left(1 - \frac{1}{\Lambda} \right) + \frac{1}{\Lambda^2} \left(1 - \frac{\alpha \text{Tr}(\underline{\underline{\tau}} \cdot \underline{\underline{\tau}})}{3G^2} \right), \tag{10}$$

and

$$\Lambda = \sqrt{1 + \frac{\text{Tr}(\underline{\underline{\tau}})}{3G}}, \tag{11}$$

$$r = \frac{\lambda_b}{\lambda_s}, \tag{12}$$

$$\nu = \frac{2}{q}, \tag{13}$$

where Λ is the backbone tube stretch, defined as the length of the backbone tube divided by the length at equilibrium, $\underline{\underline{I}}$ is the unit tensor, λ_b is the relaxation time of the backbone tube orientation (equal to the linear relaxation time), λ_s is the relaxation time for the stretch, α a parameter defining the amount of isotropy, ν a parameter signifying the influence of the surrounding polymer chains on backbone tube stretch, and q represents

the number of arms at the ends of the backbone. For this study, we use two values of q , i.e., $q=1$ to represent linear melts, and $q=5$ to represent branched melts. The value of $q=5$ is chosen so as to attain extensional thickening behavior typical of branched polymeric melts, while ensuring that the model produces monotonic shear stress as a function of Wi . The model parameters used in this study are contained in Table I(c).

It is worth noting that using the aforementioned definition of backbone stretch [see Eq. (15)], the computations stop if $Tr(\underline{\underline{\tau}})/3G < -1$, which is aphysical since $Tr(\underline{\underline{\tau}})$ should be positive. This has been shown to occur before at the front and back stagnation points in the flow around a cylinder at sufficiently high Wi [Verbeeten *et al.* (2002)]. This problem can be obviated by rewriting the backbone stretch equation as a double-equation XPP model and in this paper we implement the XPP model in an equivalent double-equation fashion, i.e., we express the polymeric stress explicitly in terms of the backbone stretch (Λ) and the orientation tensor ($\underline{\underline{Q}}$) as

$$\underline{\underline{\tau}} = 3G\Lambda^2\underline{\underline{Q}} - G\underline{\underline{I}}. \quad (14)$$

The evolution equations for the orientation tensor and the backbone tube stretch are given by

$$\begin{aligned} \underline{\underline{u}} \cdot \underline{\underline{\nabla}} \underline{\underline{Q}} - \underline{\underline{\nabla}} \underline{\underline{u}}^T \cdot \underline{\underline{Q}} - \underline{\underline{Q}} \cdot \underline{\underline{\nabla}} \underline{\underline{u}} + 2(\underline{\underline{D}} : \underline{\underline{Q}}) \underline{\underline{Q}} \\ + \frac{1}{\lambda_b \Lambda^2} \left(3\alpha \Lambda^4 \underline{\underline{Q}} \cdot \underline{\underline{Q}} + [1 - \alpha - 3\alpha \Lambda^4 Tr(\underline{\underline{Q}} \cdot \underline{\underline{Q}})] \underline{\underline{Q}} - \frac{1-\alpha}{3} \underline{\underline{I}} \right) = 0, \end{aligned} \quad (15)$$

$$\dot{\Lambda} = \Lambda(\underline{\underline{D}} : \underline{\underline{Q}}) - \frac{\exp \frac{2}{q}(\Lambda - 1)}{\lambda_s} (\Lambda - 1). \quad (16)$$

Under shear flow, the XPP model, like the FENE-P and Giesekus model, displays shear thinning behavior. The first normal stress coefficient decreases at higher shear rates, while the second normal stress coefficient is nonzero and negative. In steady extensional flow, however, unlike the FENE-CR, FENE-P and Giesekus models, XPP ($q=5$) displays a region of extensional hardening, followed by a region of mild extensional thinning. This behavior is typical of branched polymeric melts [Verbeeten *et al.* (2001, 2002)]. Setting $q=1$ results in a very small amount of extensional hardening and hence the XPP model with $q=1$ can be used to model the behavior of linear entangled polymeric systems. Under transient planar extensional flow, the XPP model displays a monotonic increase in the extensional viscosity with increasing strain for both $q=1$ and $q=5$. It is also worth noting, that for values of α greater than zero, the steady shear and transient and steady planar extensional behavior is independent of the value of α .

D. Boundary conditions

The free surface boundary conditions are the kinematic condition

$$\underline{\underline{u}} \cdot \underline{\underline{n}} = 0, \quad (17)$$

the normal stress balance

$$\underline{\underline{n}} \cdot (\underline{\underline{\tau}} - \underline{\underline{I}}P) = \frac{\underline{\underline{\nabla}}_s \cdot \underline{\underline{n}}}{Ca}, \quad (18)$$

and the vanishing shear stress

$$\underline{n} \cdot \underline{\tau} \cdot \underline{t} = 0, \quad (19)$$

where \underline{n} and \underline{t} are the unit vectors normal and tangent to the free surface respectively and ∇_s denotes the surface divergence operator. The governing equations are solved by considering a coordinate system that moves at the same speed as the bubble tip. In this reference frame the corresponding boundary conditions are the no slip condition on the solid wall,

$$u = 1, v = 0; y = 0, 0 \leq x \leq \infty, \quad (20)$$

symmetry conditions at the centerline,

$$\tau_{yy} = 0, v = 0; y = \frac{1}{2}, 0 \leq x \leq x_c \quad (21)$$

$$x_c, u = 0, \quad (22)$$

where x_c refers to the x coordinate of the bubble tip. At the outflow, a fully developed velocity profile is assumed in the thin film, i.e.,

$$\frac{\partial^2 u}{\partial y^2} = 0, \quad (23)$$

while far from the air fluid interface the velocity profile takes on the following form for the FENE-CR model [Lee *et al.* (2005), Reinelt and Saffman (1985)]:

$$u = 6(1 - 2h_\infty[1 - (h_\infty)^2])y(y - 1) + 1, v = 0. \quad (24)$$

The quantity h_∞ is the dimensional thickness of the hydrodynamic coating left behind by the advancing air bubble, and its value is determined as part of the solution. For the rest of the models (FENE-P, Giesekus, XPP) the velocity profiles are dictated by nonlinear differential equations that are solved numerically. Specifically, at the inflow, a unidirectional shear flow [$u=F(y)$] is assumed and for each model the conformation tensors are evaluated using the corresponding constitutive equations [Giesekus (1982), Bhatara *et al.* (2004); Sureshkumar *et al.* (1997), Lee *et al.* (2002), Arora *et al.* (2004)] (see Appendix A for details).

All the boundary conditions specified above are essential boundary conditions, i.e., they replace the respective governing equations at the boundary nodes, with the exception of $\underline{n} \cdot \underline{\sigma} \cdot \underline{n}$ which is imposed naturally.

E. Coupled DEVSS finite element–pseudosolid formulation

The stabilized FEM formulation used in this study is the scheme employed previously by us [Lee *et al.* (2002), Bhatara *et al.* (2004)] and we present a brief account of it here. The DEVSS formulation proposed by Guenette and Fortin (1995), Yurun *et al.* (1995), Szady *et al.* (1995), Talwar and Khomami (1992) is used to discretize the fluid governing equations. A standard Galerkin formulation is used to discretize the momentum and continuity equations. The streamline upwind Petrov-Galerkin method (SUPG) proposed by Brooks and Hughes (1982) is used to integrate the constitutive equations. The FEM formulation is coupled to the pseudo-solid domain mapping technique developed by Sackinger *et al.* (1996) and Cairncross *et al.* (2000)). The mesh is treated as a fictitious elastic solid, which deforms in response to boundary loads. As the mesh boundary con-

forms to the domain occupied by the fluid, the mesh interior moves as though it were a compressible elastic solid, and the boundary conditions relate the actual free surface problem to the pseudosolid formulation.

The residual equations obtained via the FEM formulation [Lee *et al.* (2002), Bhatara *et al.* (2004)] are solved via the Newton's iteration method, with first order continuation in both Ca and Wi . In this study, we employ the finest mesh used in our previous studies for the FENE-CR model, for which it was shown to be sufficiently refined [Bhatara *et al.* (2004)]. Since introducing shear thinning or reducing extensional thickening results in reduced stresses in the stress boundary layer in the capillary transition region as well as the tip of the bubble, we expect the chosen discretization to perform extremely well (i.e., produce converged results) for the remaining constitutive models considered.

III. FLOW FIELD COMPARISONS

A. Newtonian flow field

In the Newtonian flow, as the Ca is increased, the film thickness is also increased [Lee *et al.* (2002), Bhatara *et al.* (2004)]. The monotonic increase of the film thickness with Ca occurs because as the Ca is enhanced, the viscous drag on the fluid increases and propels more fluid into the thin film region [Ro and Homsy (1995), Lee *et al.* (2002), Bhatara *et al.* (2004)]. As the Ca is increased the recirculation region disappears and we obtain a complete bypass flow. The transition from the recirculation flow to the bypass flow occurs at a Ca of about 0.85. To further quantify the flow field we calculate the effective strain or the second invariant of the strain rate tensor (W) and the extensional rate (E), defined as

$$W = \frac{1}{2}(e_{ij}e_{ij} - e_{kk}^2), \quad (25)$$

$$E = \frac{(e_{ij}e_{ji})^{1/2}}{(e_{ij}e_{ji})^{1/2} + |(\omega_{ij}\omega_{ji})^{1/2}|}, \quad (26)$$

where e_{ij} is the strain tensor and ω_{ij} is the vorticity tensor.

As Ca is increased, the maximum effective strain rate (that occurs at the wall below the thin film) is reduced. This is attributed to the increase in the hydrodynamic film thickness with increasing Ca .

B. Viscoelastic flow field

Figure 2 illustrates the effect of elasticity on the flow field for a variety of fluids at different Ca . At low Ca , for all fluids (FENE-CR, FENE-P, Giesekus and XPP), there is a recirculation region, as observed in the Newtonian flow [see Figs. 2(a) and 2(c)]. However, for the same Ca , the effect of addition of elasticity or increasing the Wi is a decrease in the strength of the recirculation region and drawing of the lateral stagnation lines towards the vertex of the bubble [Lee *et al.* (2002), Bhatara *et al.* (2004)]. At Ca of order unity, the recirculation region disappears and a complete bypass flow is obtained [see Figs. 2(e) and 2(g)].

For both recirculation and bypass flow, the maximum effective strain rate for viscoelastic flow is a function of the deviation in the film thickness from the Newtonian case. As in the Newtonian flow, the maximum strain rate is observed at the wall in the thin film region (see Figs. 2(b), 2(d), 2(f), and 2(h)). High strain rates are also observed close to the interface in the capillary transition region. The latter region is of more

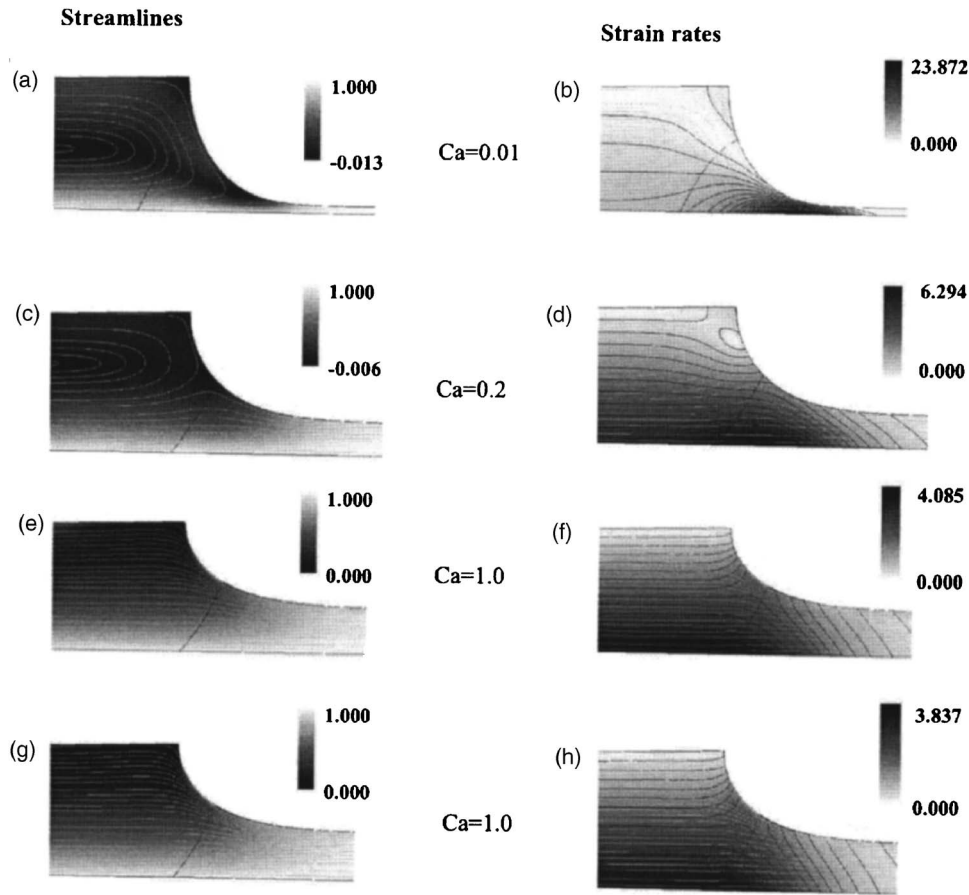


FIG. 2. Contours of the streamlines and effective strain rate at $Wi=0.6$ for different Ca : (a), (b) FENE-P ($L=10$), $Ca=0.01$; (c), (d) Giesekus ($\alpha=0.5$), $Ca=0.2$; (e), (f) XPP ($q=5$), $Ca=1.0$; (g), (h) FENE-P ($L=10$), $Ca=1.0$.

interest since it directly affects the stresses at the interface. It is observed that as the film thickness increases, the strain rate (both at the wall and near the free surface) reduces [see Figs. 3(a) and 3(b)]. Furthermore, the strain rate scales with the film thickness, i.e., the product of the maximum effective strain rate and the deviation in film thickness from the Newtonian case as a function of Ca can be nearly collapsed onto a single curve [see Fig. 3(c)], indicating that there is a direct correlation between film thickness and strain rates. Further evidence of this can be seen in Fig. 3(b) which shows the maximum effective strain rate as a function of Wi at $Ca=0.2$. For the dilute solutions [FENE-CR, FENE-P and Giesekus ($\alpha=0.01$) fluids], the semidilute solution [Giesekus ($\alpha=0.1$) fluid], and the branched polymeric melt [XPP ($q=5$) fluid] that are extensional hardening, the strain rate initially increases at low Wi and then decreases as Wi is increased. For the fluids that are not extensional hardening, i.e., the concentrated solution [Giesekus ($\alpha=0.5$) fluid] and the linear polymeric melt [XPP ($q=1$) fluid], the strain rate steadily increases with Wi . We subsequently show that the film thickness curves follow similar trends [i.e., film thickening as Wi is increased, except for the Giesekus ($\alpha=0.5$) and XPP ($q=1$) fluids, that remain film thinning].

To precisely correlate the flow dynamics to the rheological properties of the various

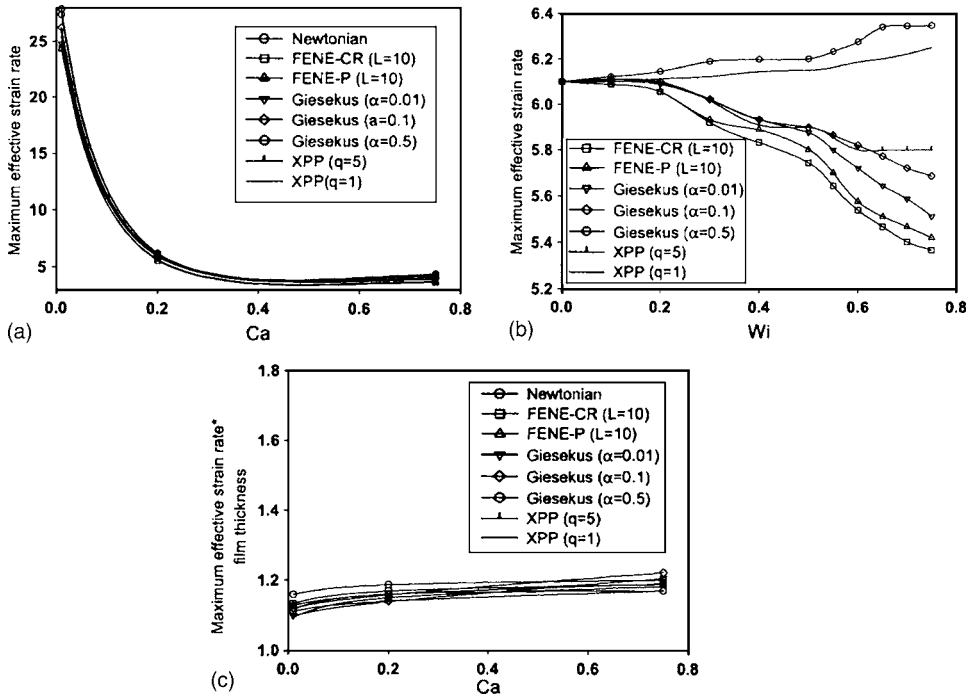


FIG. 3. (a) Variation of maximum effective strain rate with Ca at $Wi=0.6$, (b) Variation of maximum effective strain rate with Wi at $Ca=0.2$, (c) Variation of maximum strain rate scaled with film thickness with Ca at $Wi=0.6$.

fluids, we analyze the two flow regimes separately, starting with the recirculation flow and then proceeding to the bypass flow, with particular emphasis on the recirculation flow as it is most often encountered under a variety of processing conditions [Lee *et al.* (2002), Bhatara *et al.* (2004), Giavedoni *et al.* (1997)].

IV. FILM THICKNESS AND INTERFACE DYNAMICS

A. Recirculation flow

Ro and Homsy (1995), by employing a low Wi asymptotic analysis of the Oldroyd-B model, have shown that at low Ca , the presence of elasticity will result in a small film thinning effect. To understand the mechanism of film thinning, we briefly elucidate the mechanism proposed by Ro and Homsy. The authors found that film thickness is determined by two major competing forces, normal stress gradients in the flow direction (i.e., $\partial\tau_{xx}/\partial x$), and shear stress gradients (i.e., $\partial\tau_{xy}/\partial y$) in the gap direction. If the normal stress gradients are positive, they would act to assist the passage of fluid elements into the thin film region and result in film thickening. The shear stress gradients are the viscous stresses responsible for dragging the fluid elements in the direction of the wall velocity and hence forming the hydrodynamic coating (see Fig. 4). In the limit of small Ca and Wi , the authors show that film thinning results due to the presence of negative normal stresses in the flow direction, i.e., $\partial\tau_{xx}/\partial x < 0$, that are greater than the shear stress gradients. This phenomena has been observed in the large scale flow simulations conducted by [Lee *et al.* (2002) and Bhatara *et al.* (2004)].

As Wi is increased beyond the scope of Ro and Homsy's asymptotic theory, for the

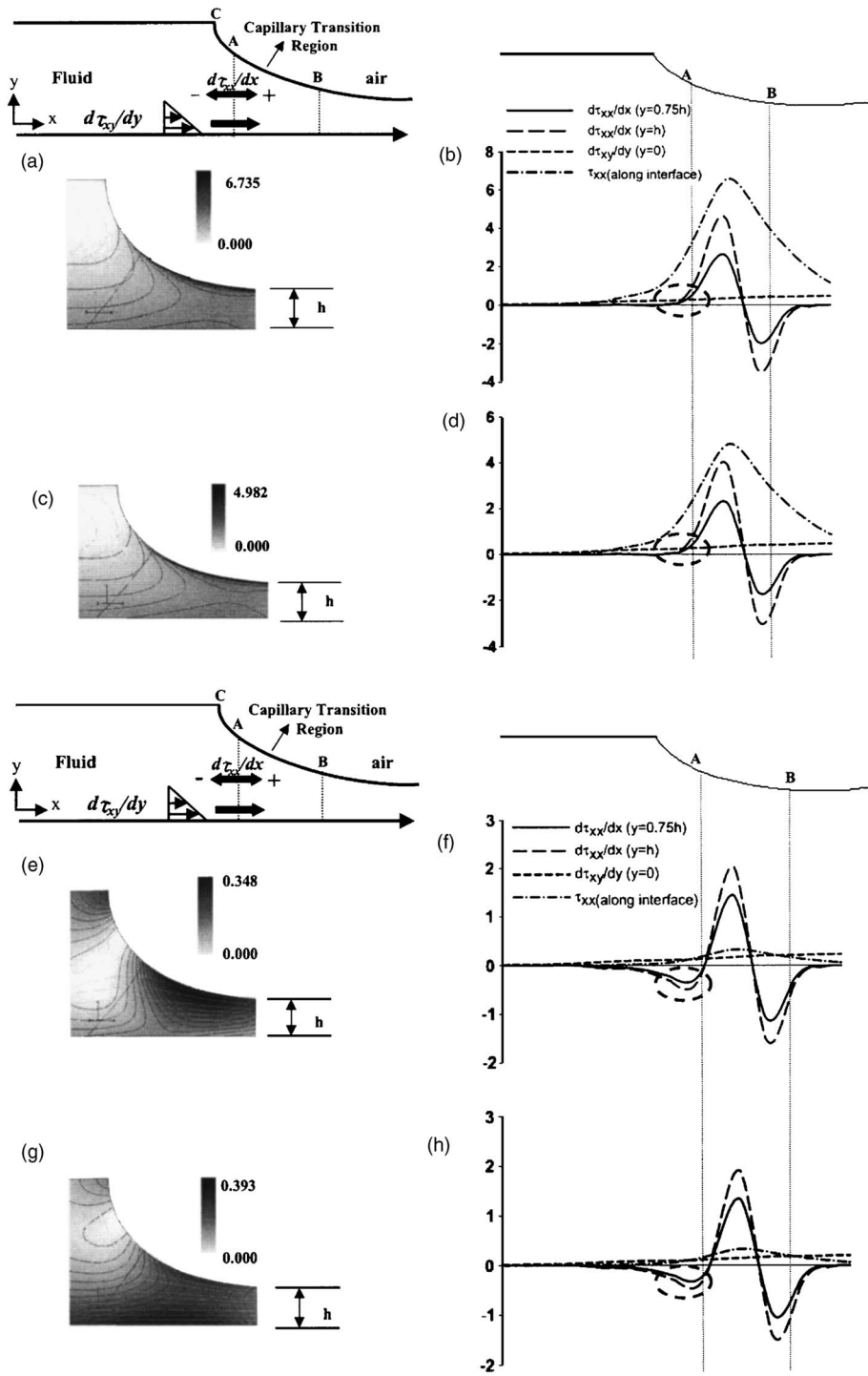


FIG. 4. Contour plots of τ_{xx} and line plots of stress and stress gradients at $Wi=0.6$, $Ca=0.2$. A marks the location of the interface stagnation point, and B the point at which free surface gradient (dh/dx) falls below 10^{-5} : (a), (b) Giesekus ($\alpha=0.01$); (c), (d) XPP ($q=5$); (e), (f) Giesekus ($\alpha=0.5$); (g), (h) XPP ($q=1$).

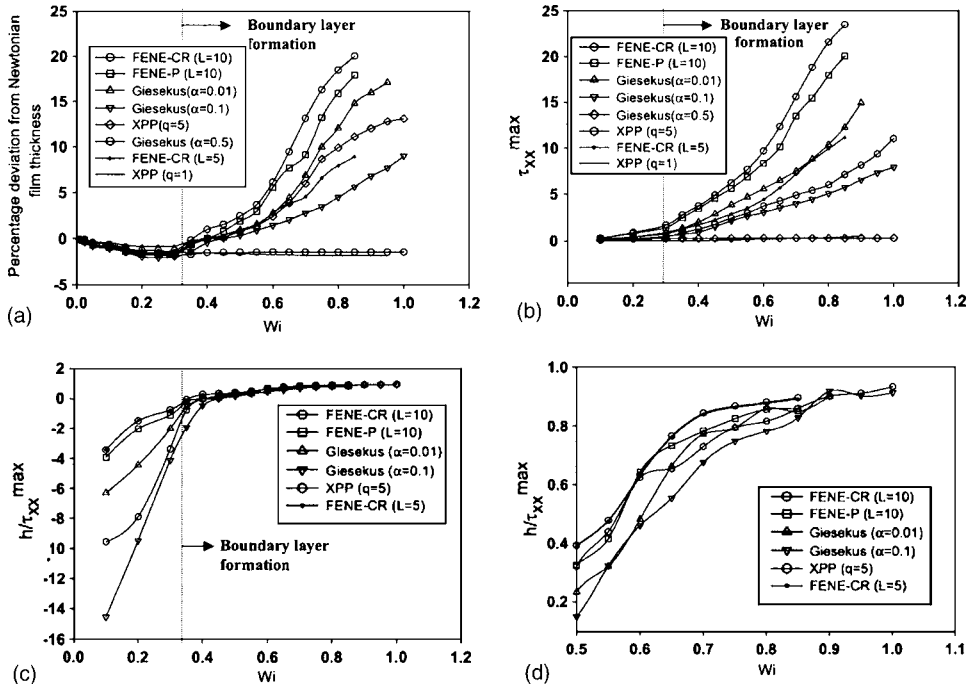


FIG. 5. (a) Percentage deviation from Newtonian film thickness with Wi at $Ca=0.2$; (b) Maximum normal stress (τ_{xx}^{max}) in the stress boundary layer as a function of Wi at $Ca=0.2$; (c), (d) Film thickness scaled with τ_{xx}^{max} as a function of Wi at $Ca=0.2$.

FENE-CR fluid, there is a film thickening effect [Lee *et al.* (2002), Bhatara *et al.* (2004)]. The film thickening is accompanied by the formation of a steep normal stress boundary layer in the capillary transition region that results in positive normal stress gradients ($\partial\tau_{xx}/\partial x > 0$), that drag more fluid into the thin film region. Similar trends are observed for the other extensional hardening fluids, i.e., the FENE-P, Giesekus ($\alpha=0.01, 0.1$), and the XPP ($q=5$) fluids [see Figs. 5(a)–5(d)]. However, the amount of film thickening depends on the extensional hardening of the fluid, and is largest for the most extensional hardening fluid. More specifically, at the same Wi , the FENE-CR ($L=10$) fluid shows the largest film thickness (highest deviation from Newtonian film thickness), followed in order, by the FENE-P, Giesekus ($\alpha=0.01$), XPP ($q=5$) and Giesekus ($\alpha=0.1$) fluids. These trends are illustrated in Fig. 6(a). Furthermore, reducing the extensibility parameter for the FENE-CR fluid, from $L=10$ to $L=5$, results in a dramatic decrease in the amount of film thickening. The fluids that are not extensional hardening, i.e., the Giesekus ($\alpha=0.5$) and XPP ($q=1$) fluids, do not display film thickening, infact they display a strong film thinning effect. This is due to the fact that in the entire Wi range explored, the normal stress gradient in the capillary transition region is negative and larger than the shear stress gradients, hence resulting in a film thinning effect [see Figs. 5(e)–5(h)].

Contours of the polymer stress (τ_{xx}) for three different fluids [FENE-CR ($L=10$), FENE-P ($L=10$) and Giesekus ($\alpha=0.01$)] with increasing Wi is displayed in Figs. 6(b), 6(d), and 6(f), respectively. At high Wi , there exists a steep stress boundary layer in τ_{xx} , due to significant stretch of the polymers downstream of the lateral stagnation line. As expected an increase in the maximum stress in the stress boundary layer, and a decrease in the thickness of the boundary layer, is achieved with increasing Wi , although both the

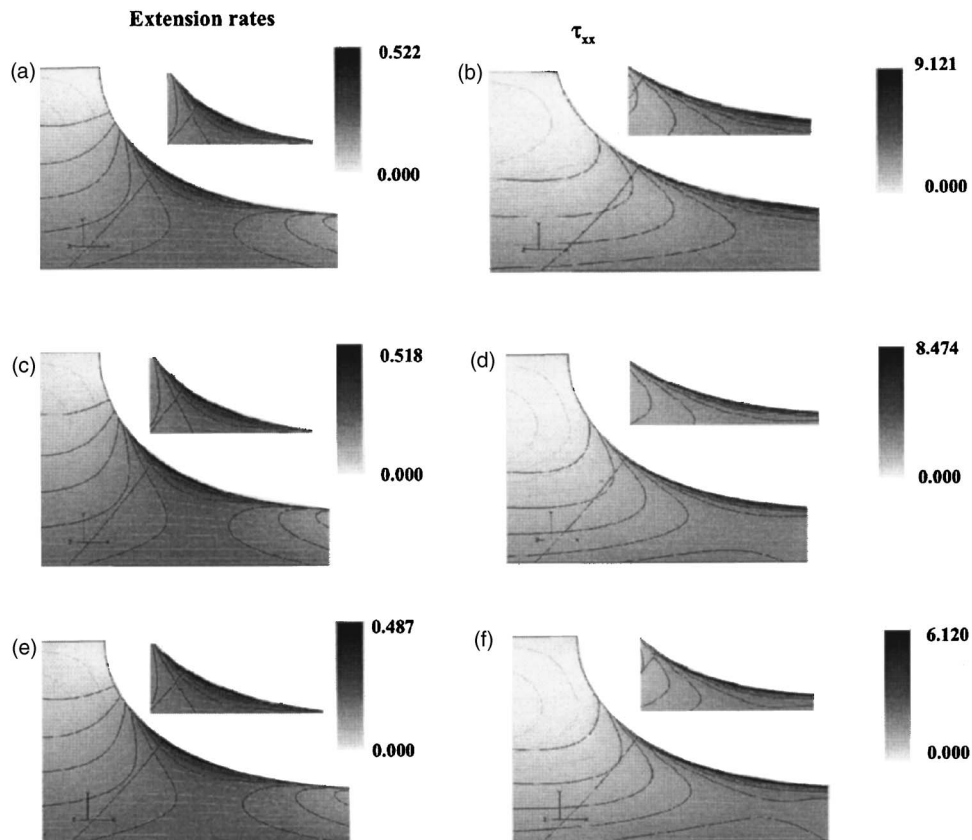


FIG. 6. Contours of the extensional rate and normal stress (τ_{xx}) at $Ca=0.2$ and $Wi=0.6$ for three different models. (a) and (b) correspond to FENE-CR ($L=10$); (c) and (d) correspond to FENE-P ($L=10$); (e) and (f) correspond to Giesekus ($\alpha=0.01$).

magnitude of the stress in the stress boundary layer, and the thickness of the stress boundary layer depend on the extensional hardening of the fluid [see Fig. 6(b)]. At the same Wi , the magnitude of the maximum normal stress follows the same order with respect to the choice of the fluid as the film thickness, i.e., the largest stresses and the steepest boundary layer are obtained for the most extensional hardening fluids and reduce with decreasing extensional hardening. The Giesekus ($\alpha=0.5$) and XPP ($q=1$) fluids, that do not display any significant extensional hardening, do not show the formation of any significant stresses at the interface in the capillary transition region as expected [see Fig. 6(b)].

The formation of the stress boundary layer occurs due to the highly convergent nature of the flow field in the capillary transition region. Since it is only the fluid elements near the free surface that are affected, we propose that the formation of the stress boundary layer is a local phenomenon, dictated by the extensional characteristics of the interface. An examination of the streamlines and the extension rates shows that there is a region of high extension rates located close to the interface in the capillary transition region (where the flow is largely a planar extensional flow), while a shear dominated mixed kinematics flow exists elsewhere. Further evidence suggesting that the normal stresses in the stress

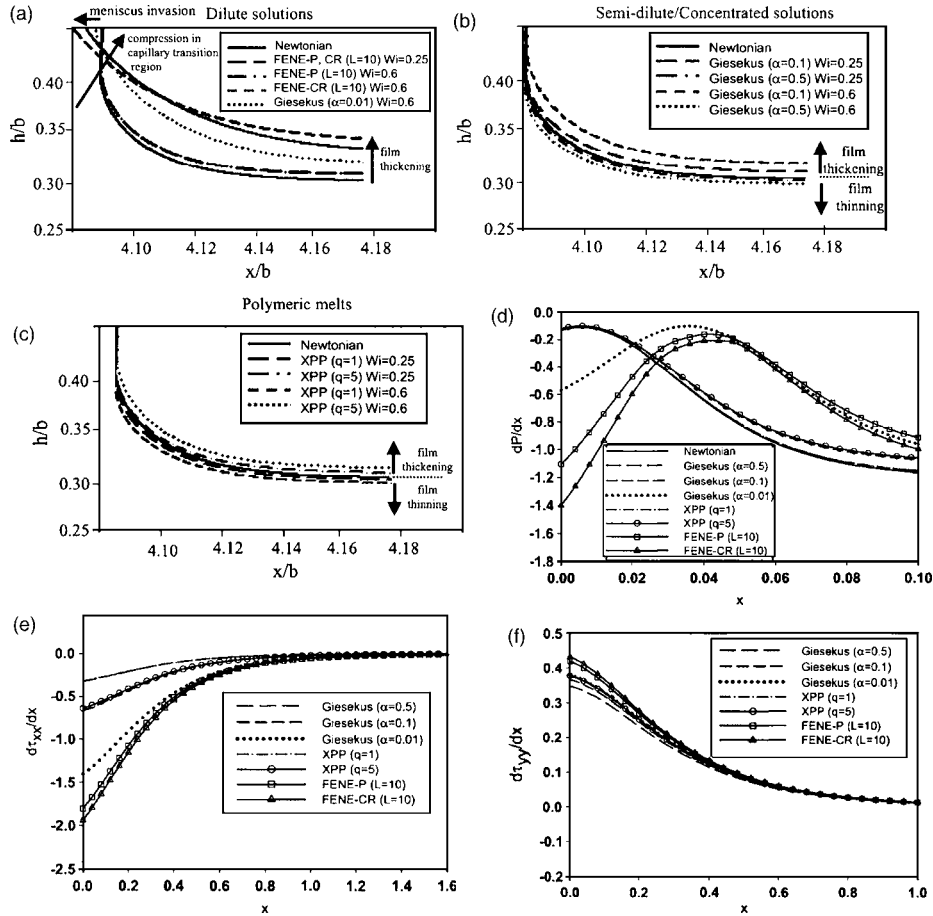


FIG. 7. Plots of the free surface shape at $Ca=0.2$, $Wi=0.6$: (a) Dilute solutions; FENE-CR ($L=10$), FENE-P ($L=10$), and Giesekus ($\alpha=0.01$) fluids; (b) semidilute/concentrated solutions; Giesekus ($\alpha=0.1, 0.5$) fluids; (c) polymeric melts; XPP ($q=1, 5$) fluids; (d) pressure gradient along the plane of symmetry at $Ca=0.2$, $Wi=0.6$; (e) normal stress gradient ($\partial\tau_{xx}/\partial x$) along the plane of symmetry at $Ca=0.2$, $Wi=0.6$; (f) normal stress gradient ($\partial\tau_{yy}/\partial x$) along the plane of symmetry at $Ca=0.2$, $Wi=0.6$. In all plots x is the distance along the symmetry line measured from the tip of the bubble.

boundary layer is a result of the extensional flow at the interface is obtained by an examination of the contours of the extension rates, that are similar to and closely parallel the contours of τ_{xx} near the free surface [see Figs. 6(a)–6(f)].

As the Wi is increased the shape of the interface goes through a series of transitions. At low Wi , the bubble adopts a circular front. The effect of increasing Wi is to deform the shape of the bubble cap by drawing the interface towards the tip of the bubble and leading to an increased compression in the capillary transition region. This has been observed before for the FENE-CR fluid [Bhatara *et al.* (2004)], and is also true for the other extensional hardening fluids, i.e., the FENE-P, Giesekus ($\alpha=0.01, 0.1$), and XPP ($q=5$) fluids [see Figs. 7(a)–7(c)]. The amount of compression depends on the extensional hardening of the fluid and reduces as the extensional hardening is decreased. As the Wi is increased further, dilute solutions [FENE-CR, FENE-P and Giesekus ($\alpha=0.01$) fluids] display a meniscus invasion phenomenon, wherein the tip of the bubble is drawn into the fluid and the free surface shape is markedly different from the Newtonian

free surface shape [see Fig. 7(a)]. These observations are consistent with experimental observations for dilute solutions [Lee *et al.* (2004)]. Furthermore, the meniscus invasion phenomenon is accompanied by a steep local pressure gradient near the tip of the bubble that is enhanced as Wi is increased [see Fig. 7(d)]. This local pressure gradient quickly dissipates as one moves away from the tip of the bubble and is followed by a monotonic decrease in the pressure [Bhatara *et al.* (2004)]. The semidilute/concentrated solutions [the Giesekus ($\alpha=0.1, 0.5$) fluids] and polymeric melts [the XPP ($q=1, 5$) fluids] do not display the phenomenon of meniscus invasion [see Figs. 7(b) and 7(c)] as the normal stresses in the stress boundary layer never get large enough in these fluids due to lack of significant extensional hardening.

It has been shown previously that the presence of elasticity results in three major competing forces at the bubble tip [Bhatara *et al.* (2004)], a reduction in strain rate due to polymeric restoring forces that result in reduced viscous normal stresses, an increased pressure drop [see Fig. 7(d)], and accumulation of elastic normal stresses near the central stagnation line [see Figs. 7(e) and 7(f)]. The pressure modification is related to the maximum normal stress in the stress boundary layer in the capillary transition region, and the steep local pressure gradient is only observed for highly extensional hardening fluids. We expect these forces to play a significant role in the stability characteristics of the flow. Furthermore, the steep local pressure gradient and the accompanying meniscus invasion observed for the highly extensional hardening fluids is most likely related to the cusping instability observed by Lee *et al.* (2005).

As stated earlier, we have shown previously, by employing diverging channel walls, that both film thickening and the boundary layer stress formation are largely independent of bulk dynamics [Bhatara *et al.* (2004)]. Furthermore, the film thickness normalized with the maximum stress in the stress boundary layer in the capillary transition region collapses onto a single universal curve (for all diverging channels), thereby suggesting that the film thickening is driven by the maximum stress in the elastic stress boundary layer at the free surface. We explore this correlation further by plotting the normalized film thickness for the different extensional hardening fluids, as a function of Wi . Once the stress boundary layer forms (at a Wi of about 0.25), the normalized film thickness for the FENE-CR ($L=10$, and $L=5$) fluid collapse onto a single curve [see Fig. 5(c)]. The normalized film thickness for the remaining fluids also nearly collapse onto the same universal curve, although a closer examination of the high Wi region shows that there are some deviations [see Fig. 5(d)]. We attribute the deviations in the FENE-P, Giesekus and XPP fluids to the shear thinning viscosity that is absent in the FENE-CR fluid. The reduction in film thickening because of shear thinning viscosity will be discussed in more detail in Sec. V.

B. Bypass flow

As in the recirculation flow, the extensional hardening fluids, i.e., the FENE-CR, FENE-P, Giesekus ($\alpha=0.01, 0.1$) and XPP ($q=5$) fluids display a film thickening effect because of the presence of elasticity (see Fig. 8). The flow displays a steady monotonic increase in film thickness with increasing Wi , with the FENE-CR ($L=10$) fluid displaying the highest deviation from the Newtonian film thickness, and the Giesekus ($\alpha=0.1$) fluid displaying the least, while both the non-extensional hardening fluids, i.e., the Giesekus ($\alpha=0.5$) and XPP ($q=1$) fluids display film thinning [see Fig. 8(e)]. The increase in film thickness with the extensional hardening fluids can be attributed to the increase in the extension rate near the bubble tip. The magnitude of the normal stresses near the tip of the bubble is now larger and can cause a change in the bubble curvature due to the normal

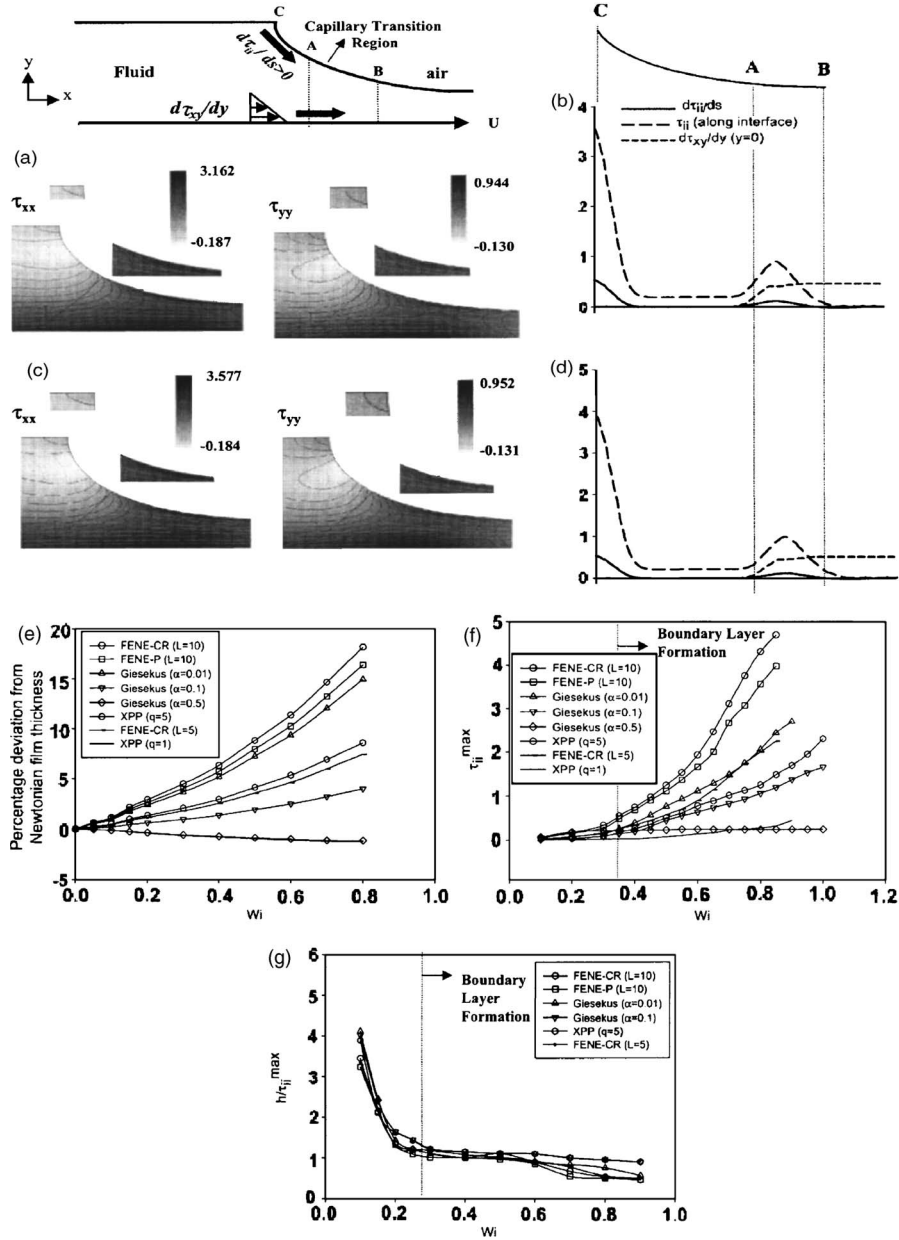


FIG. 8. Contour plots of τ_{xx} and τ_{yy} and line plots of stress and stress gradients at $Ca=1.0$ and $Wi=0.6$: (a), (b) Giesekus ($\alpha=0.01$); (c), (d) XPP ($q=5$). s is the distance along the interface measured from the tip of the bubble. (e) Percentage deviation from Newtonian film thickness with Wi at $Ca=1.0$. (f) Maximum of the trace of the stress tensor (τ_{ii}^{max}) in the stress boundary layer at bubble tip as a function of Wi at $Ca=1.0$. (g) Film thickness normalized with τ_{ii}^{max} as a function of Wi at $Ca=1.0$.

stress boundary condition. As shown previously [Bhatara *et al.* (2004)], the stress profiles obtained for the FENE-CR fluid are qualitatively very different from the stress profiles in case of the recirculation flow. The stresses at the tip of the bubble, i.e., the stagnation point, are enhanced. Even though an elastic stress boundary layer is observed in the

capillary transition region, the magnitude of normal stresses is much smaller than in the recirculation flow, because the rate of strain is smaller than in the recirculation flow, due to lack of rapid acceleration of the fluid elements into the thin film region. The formation of stress boundary layers at the stagnation point and in the capillary transition region occurs at lower Wi for the bypass flow because of the strong extensional nature of the flow and higher extension rates close to the interface. An additional feature of the stress profiles is that now both the τ_{xx} and τ_{yy} components of normal stress are comparable in magnitude [see Figs. 8(a) and 8(c)]. This is because the tangent to the stagnation point, at the interface, has components of similar magnitude in both the x and y directions, and hence the conformation dyadic has finite and comparable values in both directions. As expected, the magnitude of the maximum stress in the stress boundary layer is largest for the most extensional hardening fluids, i.e., the FENE-CR ($L=10$) and FENE-P ($L=10$) fluids and smallest for the least extensional hardening fluid, i.e., the Giesekus ($\alpha=0.1$) fluid. The XPP ($q=1$) and Giesekus ($\alpha=0.5$) fluids do not display any noticeable normal stresses.

Since the magnitude of normal stresses in the stress boundary layer in the capillary transition region is small in comparison to that of the recirculation flow, the amount of compression of the bubble in the capillary transition region is smaller [see Figs. 9(a)–9(c)]. However, similar to the recirculation flow, the amount of compression of the bubble in the capillary transition region is largest for the dilute solutions and reduces as the fluid becomes less extensional hardening. Hence, it is smallest for the concentrated solution [Giesekus ($\alpha=0.5$)] and the linear polymeric melt [XPP ($q=5$)]. Furthermore, the normal stress balance at the interface now has significant contributions from the normal stresses at the bubble tip [see Fig. 9(d)]. However, unlike the recirculation flow, the normal stresses in the bypass flow for the range of Wi examined never get large enough for the meniscus invasion phenomenon to occur. This is also corroborated by the fact that elasticity does not significantly alter the local pressure distribution near the bubble tip [see Fig. 9(e)]. These observations have been previously reported for the FENE-CR fluid ($L=10$) [Bhatara *et al.* (2004)] and are reproduced for the rest of the fluids. As in the recirculation flow, shear thinning or reduction in extensional thickening results in reduced stresses in the stress boundary layer, and hence minimizes shape changes.

Unlike the recirculation flow, the film thickness is now a function of normal stresses formed both in the capillary transition region and at the tip of the bubble. However, since the normal stresses at the tip of the bubble are more dominant than the normal stresses in the capillary transition region [see Figs. 8(b) and 8(d)], the film thickness normalized with the maximum of the trace of the stress tensor (τ_{ii}^{max}) at the bubble tip nearly collapses onto a single curve once boundary layer formation sets in (i.e., for $Wi > 0.25$). This is illustrated in Fig. 8(g). As in the recirculation flow, the deviations in this collapse are more pronounced at higher Wi because of the effect of shear thinning [the normalized film thickness collapses for the FENE-CR ($L=10$) and FENE-CR ($L=5$) fluids that have the same shear viscosity and does not collapse for the remaining fluids that exhibit shear thinning viscosity]. Furthermore, since increasing Ca leads to reduced strain rates and normal stress, the film thickness in the bypass flow is a stronger function of the shear stress gradients at the wall [see Figs. 8(b) and 8(d)] and hence, more sensitive to the effects of shear thinning. We account for the reduction in film thickness because of shear thinning viscosity in Sec. V.

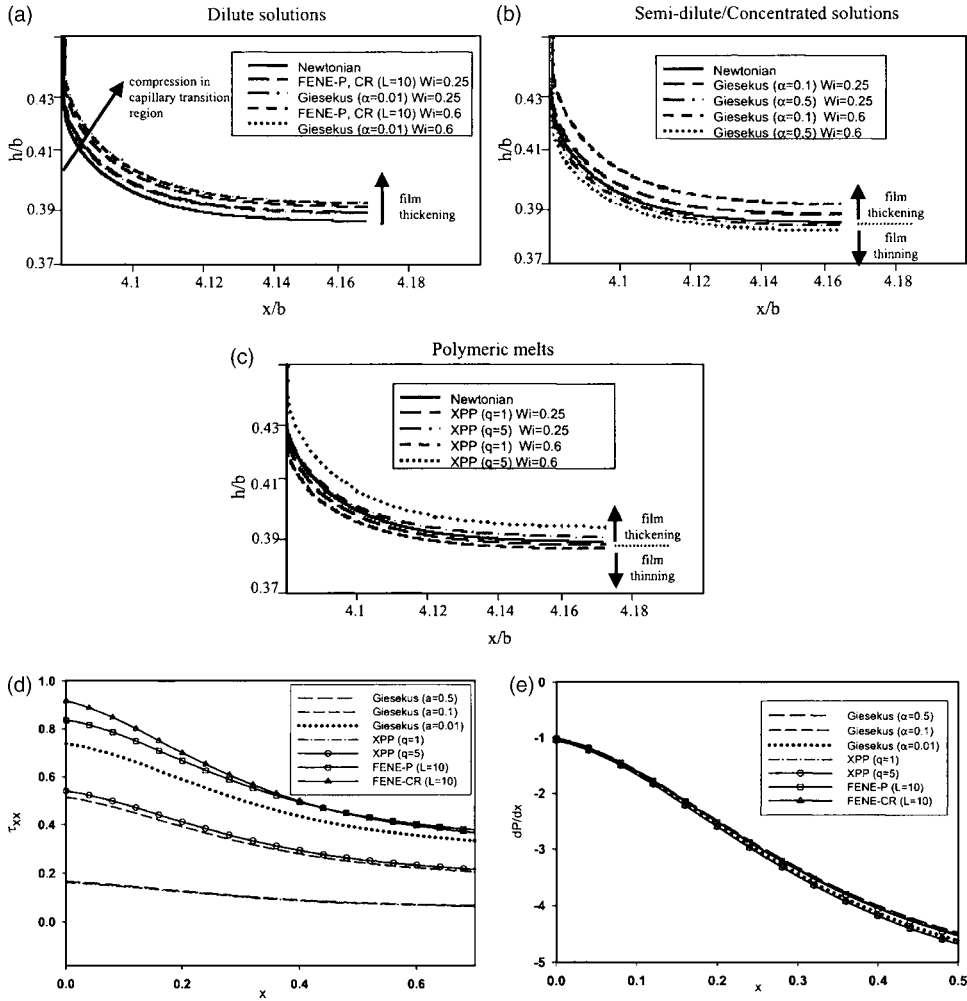


FIG. 9. Plots of the free surface shape at $Ca=1.0$, $Wi=0.6$: (a) Dilute solutions; FENE-CR ($L=10$), FENE-P ($L=10$) and Giesekus ($\alpha=0.01$) fluids; (b) semidilute/concentrated solutions; Giesekus ($\alpha=0.1, 0.5$) fluids; (c) polymeric melts; XPP ($q=1, 5$) fluids; (d) normal stress (τ_{xx}) along the plane of symmetry at $Ca=1.0$, $Wi=0.6$; (e) pressure gradient along the plane of symmetry at $Ca=1.0$, $Wi=0.6$. In all plots x is the distance along the symmetry line measured from the tip of the bubble.

V. CORRELATION OF FILM THICKNESS TO THE FLUID RHEOLOGICAL PROPERTIES

At this point we have determined that the film thickness is related to two distinct phenomena. First, the extensional hardening of the fluid, as it determines the maximum normal stress in the stress boundary layers (τ_{xx}^{max} in the recirculation flow, and τ_{ii}^{max} in the bypass flow) and the normal stress gradients ($\partial\tau_{xx}/\partial x$ in the recirculation flow, and $\partial\tau_{ii}/\partial s$ in the bypass flow). Secondly, the amount of shear thinning displayed by the fluid, as it determines the viscous drag felt by the fluid elements. In this section, we first show that we can predict the maximum normal stress in the stress boundary layer in the capillary transition region using information from the planar extensional behavior of the fluid and the flow dynamics. We then develop an accurate correlation between the film thickness

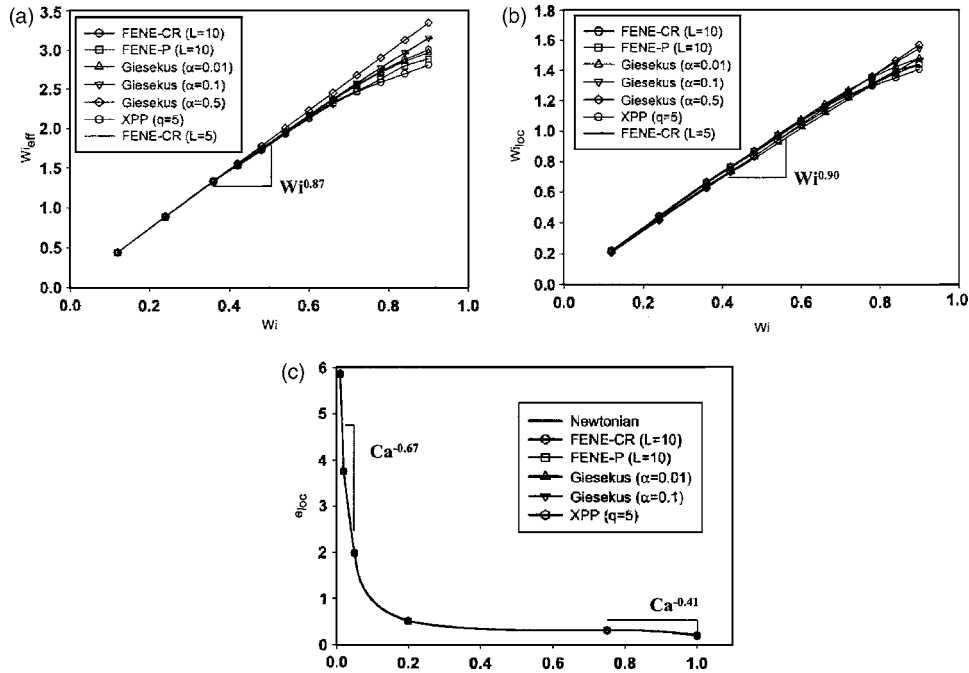


FIG. 10. (a) Plot of the effective Wi as a function of Wi at $Ca=0.2$. (b) Plot of the local Wi as a function of Wi at $Ca=0.2$. (c) Plot of the local extensional rate at the interface as a function of Ca . For the viscoelastic fluids, $Wi=0.6$.

and the maximum normal stress by incorporating the effect of shear thinning [i.e., account for the deviations in the normalized film thickness in Figs. 5(c) and 8(g)].

A. Effect of extensional hardening

For the most extensional hardening fluids [the dilute solutions, FENE-CR ($L=10$) and FENE-P ($L=10$)], we start to observe the formation of stress boundary layers and accompanying film thickening at Wi of about 0.25 at low Ca ($Ca < 1.0$). We observe a delay in the onset of the boundary layer with respect to Wi , a reduction in the maximum stress in the stress boundary layer and an increase in the thickness of the stress boundary layer as the extensional hardening of the fluid decreases. For fluids that do not display any significant extensional hardening we do not observe any noticeable normal stresses. This indicates that irrespective of the concentration and/or chain architecture, there exists a direct correlation between the formation of the stress boundary layer and extensional hardening of the fluid.

Since the flow is inhomogenous and has varying Wi in the flow domain, in order to draw precise correlations, we define an effective Wi , based on the strain rate scaling with film thickness, i.e., $Wi_{eff} = Wi * (b/h)$. The local Wi at the interface in the capillary transition region can then be defined as $Wi_{loc} = Wi_{eff} * (W_{int}/W_{max})$, where W_{int} is the strain rate at the interface where the boundary layer stresses form, and W_{max} is the maximum effective strain rate. The effective and local Wi are plotted as a function of Wi for each model at a representative value of Ca ($Ca=0.2$) in Figs. 10(a) and 10(b), respectively. Approximate scalings for both Wi_{loc} and Wi_{eff} can be obtained (i.e., $Wi_{loc} \propto Wi^{0.87}$ and $Wi_{eff} \propto Wi^{0.90}$). The similar power-law scalings for Wi_{loc} and Wi_{eff} indicates that the strain

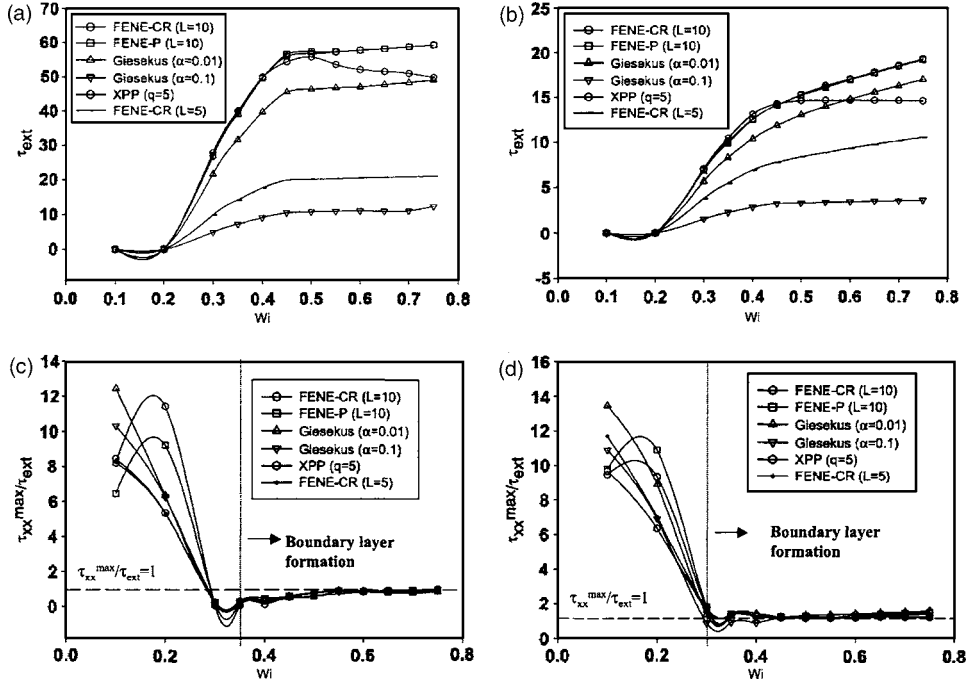


FIG. 11. (a) Plot of the calculated extensional stress as a function of Wi at a strain rate of 2. (b) Plot of the calculated extensional stress as a function of Wi at a strain rate of 0.5. (c) Plot of the ratio of the maximum normal stress (τ_{xx}^{max}) in the stress boundary layer at $Ca=0.2$ and the extensional stress calculated at a strain rate of 0.5. (d) Plot of the ratio of the maximum normal stress (τ_{xx}^{max}) in the stress boundary layer at $Ca=0.05$ and the extensional stress calculated at a strain rate of 2.0. Wi refers to the actual Wi in the free surface problem.

rate at the interface normalized with the maximum strain rate is a weak function of Wi .

We calculate the extensional stress based on the local Wi , defined as

$$\tau_{ext} = \mu_{loc} * e_{loc}, \quad (27)$$

where e_{loc} is the local extensional rate at the interface in the capillary transition region, and μ_{loc} is the extensional viscosity obtained from the steady planar extensional rheology data based on Wi_{loc} . Our simulations indicate that e_{loc} is a strong function of Ca (i.e., predominantly determined by the flow kinematics) and only weakly dependent on Wi . Consequently, approximate scalings for e_{loc} with Ca can be obtained, i.e., in the recirculation flow ($Ca < 1.0$), at low Ca , $e_{loc} \propto Ca^{-0.67}$, and at moderate to high Ca , $e_{loc} \propto Ca^{-0.41}$ [see Fig. 10(c)], while in the bypass flow ($Ca \geq 1.0$), $e_{loc} \propto Ca^{-0.36}$. The scaling at low Ca reflects the $Ca^{2/3}$ dependence of the film thickness on Ca [Ro and Homsy (1995)].

The extensional stress calculated using Eq. (27) is plotted in Figs. 11(a) and 11(b) for all fluids, as a function of the actual Wi in the free surface problem, at $Ca=0.2$. Figure 11(a) shows the extensional stresses at a strain rate of 2 (i.e., the strain rate at the interface in the capillary transition region at $Ca=0.05$), while Fig. 11(b) shows the extensional stresses at a strain rate of 0.5 (i.e., the strain rate at the interface in the capillary transition region at $Ca=0.2$). As expected, at both strain rates, the extensional stress is a function of the choice of the fluid, and is largest for the most extensional hardening fluids [FENE-CR, FENE-P ($L=10$)] and reduces with decreasing extensional hardening. The calculated extensional stress shows the same trend with Wi as the maximum normal stress in the stress boundary layer in the capillary transition region.

TABLE II. Strain values for different Ca and Wi [FENE-CR ($L=10$)].

Ca	Wi	ε
0.05	0.4	38.6
0.05	0.5	34.7
0.2	0.4	14.2
0.2	0.5	12.8
1.0	0.4	7.5
1.0	0.5	7.3
2.0	0.4	5.1
2.0	0.5	5.0
10.0	0.4	1.1
10.0	0.5	1.1

In addition to the qualitative similarities between the trend in the variation of the maximum normal stress in the stress boundary layer and the calculated extensional stress with Wi , we also observe good quantitative agreement between them. We plot the ratio of the observed maximum normal stress in the actual free surface problem, at $Ca=0.2$ to the calculated extensional stress at a strain rate of 0.5 as a function of Wi in Fig. 11(c). There is a good agreement between the values of the two quantities once boundary layer formation occurs, i.e., $\tau_{xx}^{max}/\tau_{ext} \approx 1$ [see Fig. 11(c)]. Repeating this procedure at $Ca=0.05$ (at which the strain rates are higher and consequently the maximum normal stress in the stress boundary layer is larger), we find good agreement between the maximum normal stress and the calculated extensional stress at the higher strain rate of 2.0 [see Fig. 11(d)].

The excellent predictions of normal stresses at the interface based on the steady planar extensional viscosity of the fluid suggests that the fluid elements experience a significant amount of strain at the interface above the Wi at which the stress boundary layer is formed. To verify this point, we have computed the strain on the fluid elements at the interface downstream of the stagnation point in the capillary transition region (for details see Appendix B). Clearly, in the range of Ca where a recirculation flow exists, the fluid elements experience a very large strain so the appropriate measure would be the steady planar extensional viscosity (see Table II). In the case of the bypass flow ($Ca \geq 1.0$), the strain rates are reduced. However, up to a Ca of 2.0, the strain on the fluid elements at the bubble tip is still large enough that one can use the steady planar extensional viscosity to predict the extensional stresses. As Ca is increased to a value significantly higher than 2.0, the strain on the fluid elements is small (≈ 1.0) and consideration of the transient planar extensional viscosity is an important issue in predicting the extensional stresses.

B. Effect of shear thinning

As stated previously, it is observed that the presence of shear thinning in viscosity results in reduced film thickening. This is clearly illustrated in Fig. 12(a), where we plot the ratio of the film thickness for the FENE-CR ($L=10$) and FENE-P ($L=10$) fluids, with the ratio of the shear viscosities of the respective fluids (at the same Wi or same normal stress). There is a reduction in the film thickness of about 4% when the shear viscosity is reduced by about 2% indicating the sensitivity of the film thickness to the difference in shear viscosity. Since the extensional viscosity and the first normal stress coefficient of the FENE-CR ($L=10$) and the FENE-P ($L=10$) fluids is similar at the same Ca and Wi , it is the shear thinning in the viscosity that reduces the film thickness by reducing the

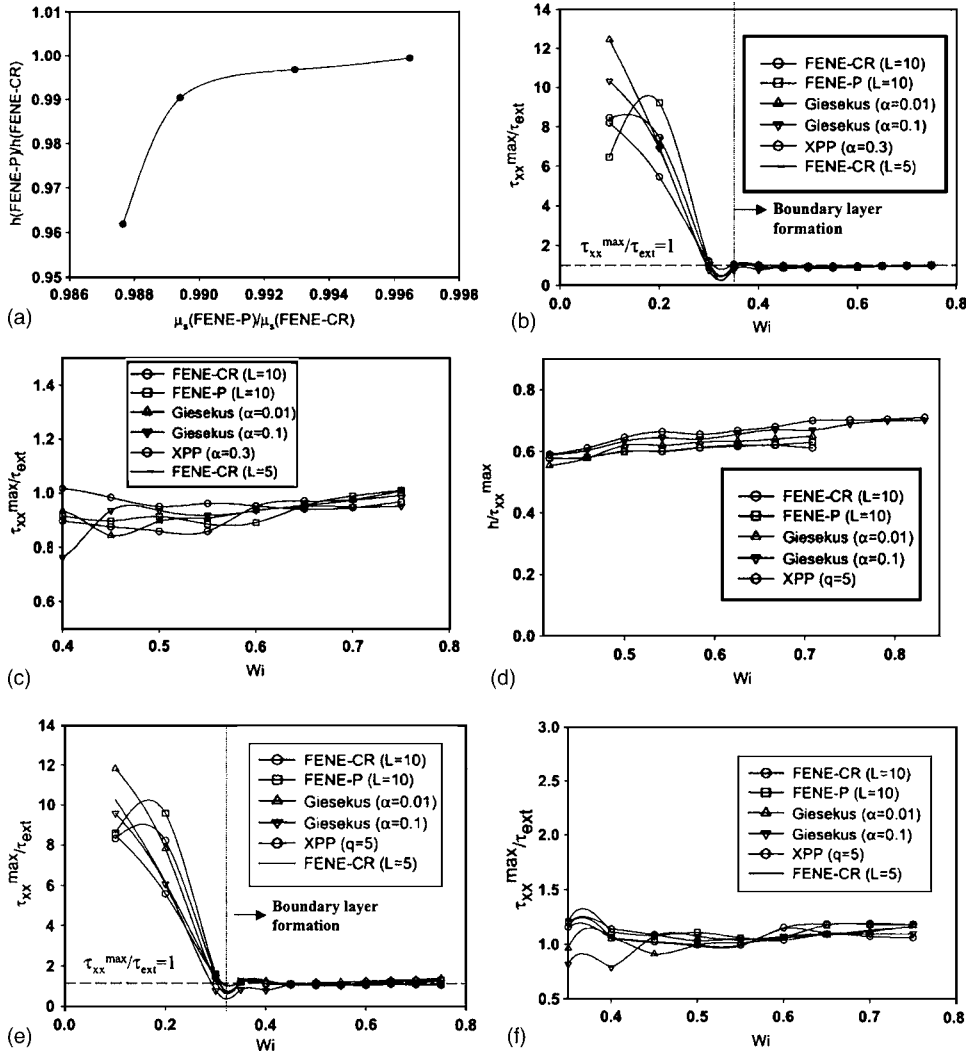


FIG. 12. (a) Plot of the ratio of film thickness for FENE-P ($L=10$) and FENE-CR ($L=10$) with the ratio of respective shear viscosities at $Ca=0.2$. (b), (c) Plot of the ratio of the maximum normal stress (τ_{xx}^{max}) in the stress boundary layer at the effective Ca and the extensional stress calculated for a strain rate of 0.5, (d) Plot of film thickness normalized with τ_{xx}^{max} at the effective Ca . (e), (f) Plot of the ratio of the maximum normal stress (τ_{xx}^{max}) in the stress boundary layer at the effective Ca and the extensional stress calculated for a strain rate of 2.0. Wi refers to the actual Wi in the free surface problem.

shear stress gradients at the wall or the viscous drag felt by the fluid elements [Ro and Homsy (1995)].

In order to account for shear thinning in the extensional hardening, shear thinning fluids, namely, the FENE-P, Giesekus ($\alpha=0.01, 0.1$) and XPP ($q=5$) fluids, we define an effective Ca based on a normalization of the viscosity with the shear viscosity at the wall shear rate (also the maximum shear rate), since the shear rate at the wall predominantly determines the amount of fluid dragged into the thin film region. The effective Ca , hence, is defined as

$$Ca_{eff} = Ca * \mu_{\gamma_{wall}}, \tag{28}$$

where $\mu_{\gamma_{wall}}$ is the dimensionless shear viscosity at the wall shear rate, and is obtained from the steady shear rheological predictions of that particular fluid. For a particular Wi , we suggest that the normal stress corresponding to Ca_{eff} can be correlated to the extensional stress calculated above. Figures 12(b) and 12(c) show the ratio of the maximum normal stress corresponding to Ca_{eff} to the calculated extensional stress (at a strain rate of 0.5) as a function of Wi . We notice a marked improvement in the agreement between τ_{xx}^{max} and the calculated extensional stress. Furthermore, the film thickness normalized with τ_{xx}^{max} corresponding to Ca_{eff} now collapses onto a single curve for all fluids [see Fig. 12(d)], thereby establishing that for Wi greater than the critical Wi for boundary layer formation, the film thickness scales with the maximum normal stress provided shear thinning is accounted for. This procedure is repeated at $Ca=0.05$ and again there is a marked improvement in the agreement between τ_{xx}^{max} and the calculated extensional stress at a strain rate of 2.0 [see Figs. 12(e) and 12(f)].

For the bypass flow, since Ca is higher, the effect of viscous drag on film thickness is more pronounced than in the recirculation flow. Hence, shear thinning has a more pronounced effect on film thickness than in the recirculation flow. However, both the maximum of the trace of the stress tensor (τ_{ii}^{max}) and the film thickness can still be collapsed with τ_{ext} by normalization with Ca_{eff} . This is illustrated in Figs. 13(a) and 13(b), respectively, where we plot the ratio of τ_{ii}^{max} with τ_{ext} (at a strain rate of 0.17 which corresponds to the extensional rate at the interface near the bubble tip at $Ca=1.0$) and the film thickness normalized with τ_{ii}^{max} corresponding to Ca_{eff} . Even though the deviations in h/τ_{ii}^{max} [see Fig. 8(g)] are significant at higher Wi , the normalized film thickness collapses onto a single curve by adjusting Ca .

For the linear polymeric melt represented by the XPP ($q=1$) constitutive equation and the concentrated solution represented by the Giesekus ($\alpha=0.5$) constitutive equation, since there is no extensional hardening, we propose that it is possible to predict the film thinning effect directly from the shear viscosity at the wall shear rate (since now it is the viscous drag that is primarily responsible for determining the film thickness). To that end, we scale the film thickness at a particular Ca and Wi with the shear viscosity at the wall shear rate, and obtain the ratio of scaled film thickness as,

$$\left(\frac{h_{Ca_0, Wi_0}}{h_{Ca_1, Wi_1}} \right) / \left(\frac{\mu_{Ca_1, Wi_1}}{\mu_{Ca_0, Wi_0}} \right). \tag{29}$$

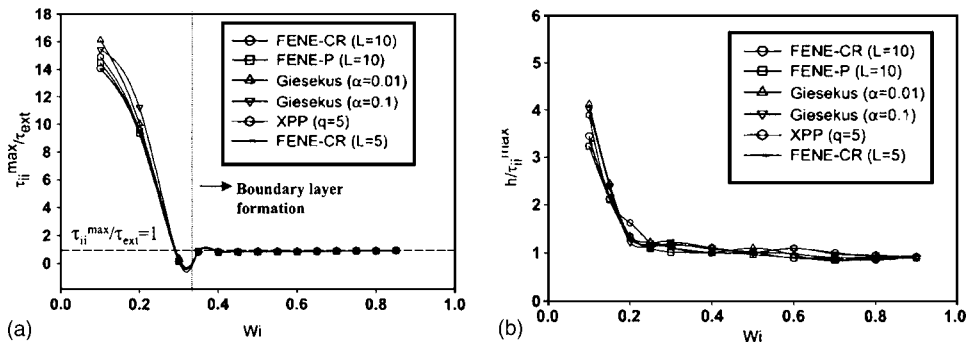


FIG. 13. (a) Plot of the ratio of the maximum trace of stress (τ_{ii}^{max}) in the stress boundary layer at $Ca=1.0$ and the extensional stress calculated at a strain rate of 0.17. (b) Plot of film thickness normalized with τ_{ii}^{max} at the effective Ca for $Ca=1.0$. Wi refers to the actual Wi in the free surface problem.

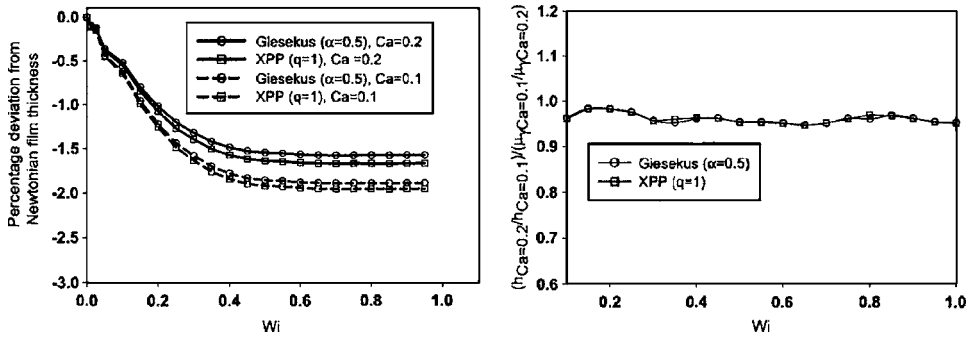


FIG. 14. (a) Plot of the film thickness with Wi for $Ca=0.2$ and $Ca=0.1$ for Giesekus ($\alpha=0.5$) and XPP ($q=5$). (b) Plot of ratio of film thickness to viscosity at different Ca . Wi refers to the actual Wi in the free surface problem.

Figure 14(a) shows the deviation in film thickness for the Giesekus ($\alpha=0.5$) and XPP ($q=1$) fluids at two different Ca (i.e., $Ca=0.1$ and $Ca=0.2$). Film thickness is reduced at lower Ca because of higher shear rates at lower Ca . Figure 14(b) shows the ratio of the scaled film thickness at $Ca=0.2$ to the scaled film thickness at $Ca=0.1$, for different Wi . For the range of Wi explored, the scaled film thickness collapses onto a single curve for both fluids, hence, indicating that the film thickness in the absence of extensional hardening can be determined solely based on the steady shear rheological characteristics of the fluid.

C. Scaling analysis

At this point, it would be helpful to provide approximate scalings for the film thickness with respect to Ca and Wi that emerge from our simulations. The objective behind this is to illustrate a way by which film thickness variations at low and moderate to high Ca can be estimated based on flow conditions and the nature of the fluid (extensional hardening versus nonextensional hardening).

From Eq. (27), the extensional stress can be expressed as a function of Wi and Ca , i.e.,

$$\tau_{ext} = \mu_{loc} * e_{loc} \approx g(Wi_{loc})k(Ca_{eff}) = g'(Wi)k'(Ca). \quad (30)$$

1. Recirculation flow

In the recirculation flow, $k'(Ca)$ has been determined to be $Ca^{-0.67}$ at low Ca , and $Ca^{-0.41}$ at high Ca [see Fig. 10(c)]. In order to determine the dependence of μ_{loc} on Wi , exponential curves are fitted to the steady planar extensional flow data in the coil-stretch transition region, i.e., $0.5 \leq Wi \leq 2.0$ (see Fig. 15). This region corresponds to the strain rates within which our calculations are performed. Further support for this can be found in the estimation of τ_{xx} for the calculated strain rates [see Figs. 11(a) and 11(b)] which suggest that we are in the coil-stretch transition regime. Furthermore, given that for the extensional hardening fluids, the film thickness scales with the extensional stresses, and for non-extensional hardening fluids, the film thickness scales with the effective Ca , one should be able to develop scalings for the film thickness. Based on our calculations at low Ca , i.e., $Ca \leq 0.2$ (see Fig. 16), we obtain scalings for film thickness with Wi and Ca [see Table III(a)]. As Ca is increased ($0.2 \leq Ca < 1.0$), the film thickness scalings now reflect a $Ca^{0.41}$ dependence, with Wi dependence remaining approximately the same.

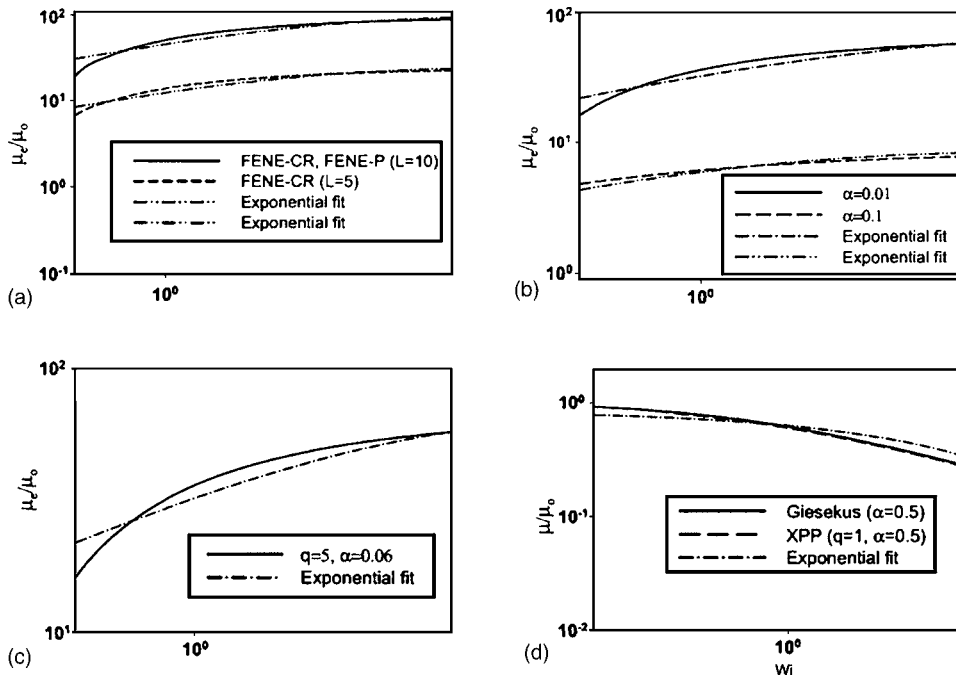


FIG. 15. Exponential fits to the steady planar rheological data. Extensional viscosity in steady planar extensional flow: (a) FENE-CR ($L=5, 10$), FENE-P ($L=10$); (b) Giesekus ($\alpha=0.01, 0.1$); (c) XPP ($q=5, \alpha=0.06$). Shear viscosity in steady shear flow: (d) Giesekus ($\alpha=0.5$); XPP ($q=1, \alpha=0.5$).

2. Bypass flow

In the bypass flow ($Ca \geq 1.0$) we again obtain scalings for film thickness with Wi and Ca [see Fig. 17 and Table III(b)]. We observe these scalings to hold true for values of Ca that are not significantly greater than 1.0. As the value of Ca is increased, the strain at the tip of the bubble decreases (see Table II). For $Ca=10.0$, the strain is low enough ($\epsilon \approx 1.0$) for the transient characteristics to be important. Hence, we expect the scaling analysis based on steady data to be insufficient in predicting film thickness at such high values of Ca .

VI. CONCLUSION

We have inspected the effect of viscoelasticity on the interfacial dynamics of a Hele-Shaw cell free surface displacement flow. The FENE-CR (extensional hardening, constant shear viscosity, shear thinning first normal stress coefficient) and the FENE-P (extensional hardening, shear thinning viscosity and shear thinning first normal stress coefficient) constitutive equations are used to model dilute polymeric solutions. The Giesekus constitutive equation ($\alpha=0.01, 0.1, 0.5$) is used to model dilute, semidilute and concentrated solutions. For all values of α , the model shows shear thinning viscosity and shear thinning first and second normal stress coefficients and for two of the α values (0.01, 0.1), the model displays significant extensional hardening. The XPP constitutive equation is used to model polymeric melts. Linear polymeric melts are represented by setting $q=1$, while branched polymeric melts are represented by setting $q=5$. For both $q=1$ and $q=5$, the model shows shear thinning viscosity and shear thinning first and second normal stress coefficients. In steady planar extensional flow the XPP ($q=5$) model

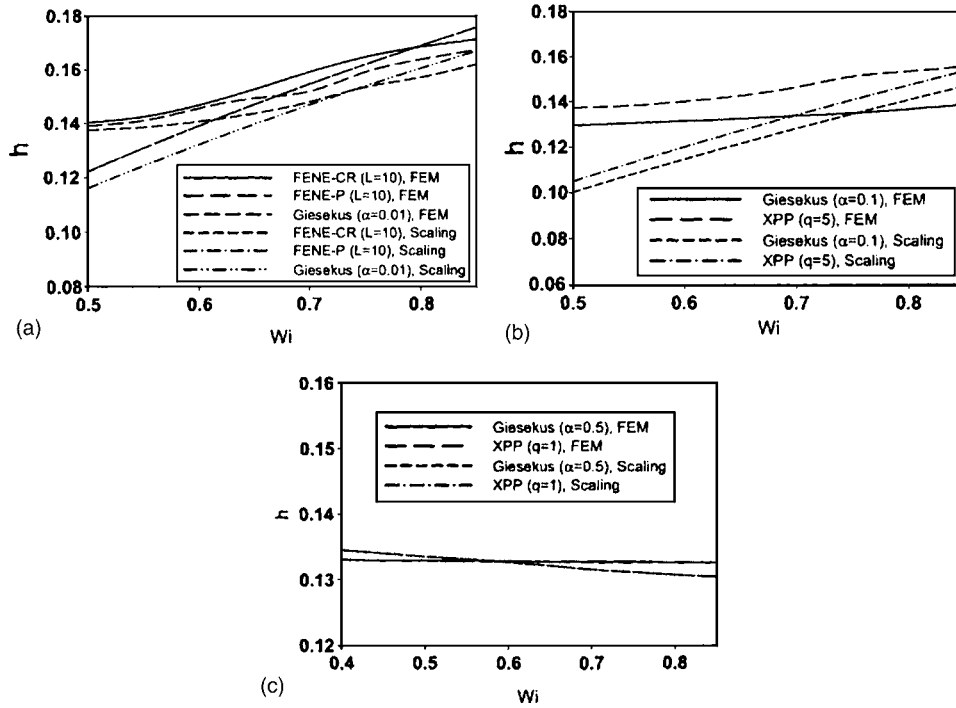


FIG. 16. Plots of the film thickness obtained from the simulations and the scaling analysis at $Ca=0.2$: (a) FENE-CR ($L=10$), FENE-P ($L=10$), Giesekus ($\alpha=0.01$); (b) Giesekus ($\alpha=0.1$), XPP ($q=5$); (c) Giesekus ($\alpha=0.5$), XPP ($q=1$).

TABLE III. Scalings for the film thickness with Wi and Ca . (a) Recirculation flow; (b) bypass flow.

(a) Recirculation flow	
Fluid	h (scaling)
Dilute solutions: FENE-CR (nonshear thinning)	$(1 - e^{-0.68Wi^{0.87}})Ca^{0.67}$
Dilute solutions: FENE-P, Giesekus ($\alpha=0.01$)	$(1 - e^{-0.68Wi^{0.87}})e^{-0.42Wi^{0.87}}Ca^{0.67}$
Semidilute solutions: Giesekus ($\alpha=0.1$)	$(1 - e^{-1.16Wi^{0.87}})e^{-0.38Wi^{0.87}}Ca^{0.67}$
Branched polymeric melts: XPP ($q=5, \alpha=0.06$)	$(1 - e^{-1.14Wi^{0.87}})e^{-0.38Wi^{0.87}}Ca^{0.67}$
Concentrated solutions and linear polymeric melts: Giesekus ($\alpha=0.5$) and XPP ($q=1, \alpha=0.5$)	$(e^{-0.31Wi^{0.87}})Ca^{0.67}$
(b) Bypass flow	
Fluid	h (scaling)
Dilute solutions: FENE-CR (nonshear thinning)	$(1 - e^{-0.59Wi^{0.87}})Ca^{0.67}$
Dilute solutions: FENE-P, Giesekus ($\alpha=0.01$)	$(1 - e^{-0.59Wi^{0.87}})e^{-0.40Wi^{0.87}}Ca^{0.36}$
Semidilute solutions: Giesekus ($\alpha=0.1$)	$(1 - e^{-1.12Wi^{0.87}})e^{-0.38Wi^{0.87}}Ca^{0.67}$
Branched polymeric melts: XPP ($q=5, \alpha=0.06$)	$(1 - e^{-0.98Wi^{0.87}})e^{-0.38Wi^{0.87}}Ca^{0.67}$
Concentrated solutions and linear polymeric melts: Giesekus ($\alpha=0.5$) and XPP ($q=1, \alpha=0.5$)	$(e^{-0.31Wi^{0.87}})Ca^{0.36}$

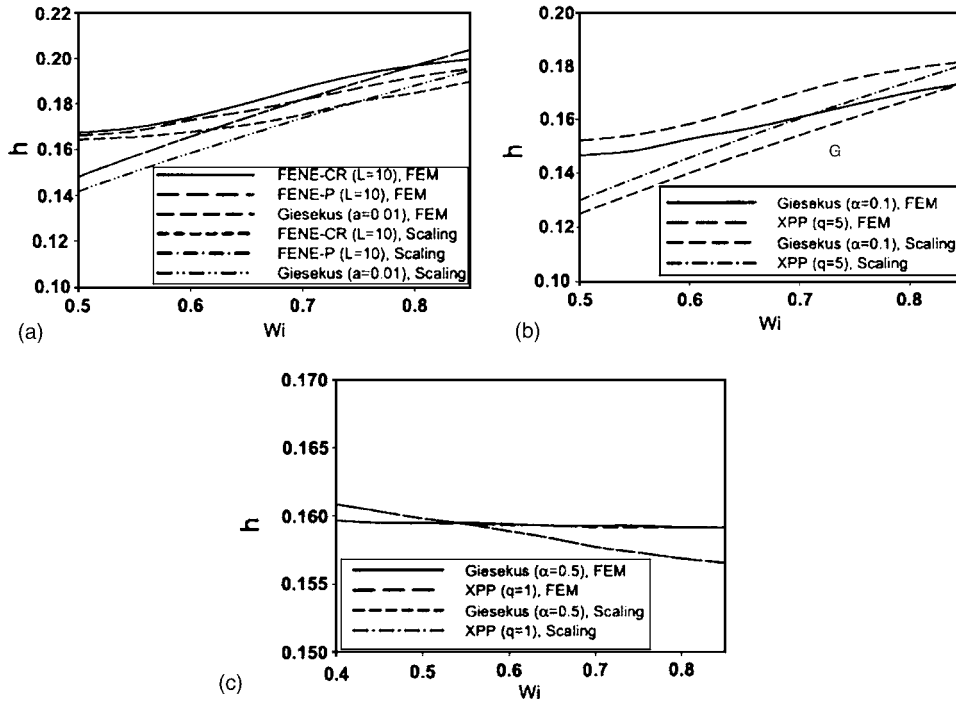


FIG. 17. Plots of the film thickness obtained from the simulations and the scaling analysis at $Ca=1.0$: (a) FENE-CR ($L=10$), FENE-P ($L=10$), Giesekus ($\alpha=0.01$); (b) Giesekus ($\alpha=0.1$), XPP ($q=5$); (c) Giesekus ($\alpha=0.5$), XPP ($q=1$).

displays a region of significant extensional hardening at lower strain followed by mild extensional thinning at higher strain, while the XPP ($q=1$) model does not display any significant extensional hardening.

In the free surface problem, regardless of the polymer concentration and chain architecture, the flow displays a recirculation pattern (the strength of which decreases with elasticity) at low Ca and a bypass flow at high Ca . In case of the recirculation flow, at low Ca and Wi , all models display a film thinning effect while at higher Ca and Wi , the extensional hardening fluids display a film thickening effect while the fluids that do not display any significant extensional hardening remain film thinning. One of the consequences of film thickening is a reduction in the maximum effective strain rate. The maximum effective strain rate scales with the film thickness for all fluids at all Ca and Wi . Furthermore, the film thickening is accompanied by the formation of elastic normal stress (τ_{xx}) boundary layers, which result in a positive normal stress gradient in the capillary transition region ($\partial\tau_{xx}/\partial x > 0$) in the flow direction. The magnitude of the maximum stress in the stress boundary layer increases with Wi . Both the film thickness and maximum normal stress are largest for the most extensional hardening fluids, i.e., the dilute solutions represented by the FENE-CR, FENE-P and Giesekus ($\alpha=0.01$) constitutive equations, and decrease as extensional hardening is decreased, and subsequently smaller for the semidilute solution represented by the Giesekus ($\alpha=0.1$) constitutive equation and the branched polymeric melt represented by the XPP ($q=5$) constitutive equation. The fluids that do not display any significant extensional hardening, i.e., the concentrated solution represented by the Giesekus ($\alpha=0.5$) constitutive equation and the linear poly-

meric melt represented by the XPP ($q=1$) constitutive equation, display film thinning and no noticeable normal stresses.

In the recirculation flow, we observe that the film thickness scales with the maximum normal stress in the stress boundary layer in the capillary transition region near the free surface. Specifically, for the extensional hardening, nonshear thinning fluids, i.e., the FENE-CR ($L=5$) and ($L=10$) fluids, the film thickness normalized with the maximum normal stress in the stress boundary layer, collapses onto a single curve. For the extensional hardening, shear thinning fluids, i.e., the FENE-P ($L=10$), Giesekus ($\alpha=0.01, 0.1$), and XPP ($q=5$) fluids, there are some slight deviations from this collapse. This is because film thickening is reduced by shear thinning which lowers the viscous forces that drag fluid into the thin film region. We show that shear thinning can be accounted for by defining an effective Ca by normalizing the viscosity with the shear viscosity at the wall shear rate. For a given Wi , the film thickness normalized with the maximum normal stress at the effective Ca now collapses onto a single curve for the aforementioned fluids. For the fluids that are shear thinning but not extensional hardening, it is observed that the film thickness scaled with the shear viscosity at the wall shear rate collapses onto a single curve, indicating that the film thickness solely depends on the viscous drag felt by the fluid elements.

For the recirculation flow, we correlate the measured film thickness and normal stresses to the rheological behavior of the fluids. Since the flow is planar extensional at the interface in the capillary transition region where the stress boundary layer forms, it is possible to calculate the maximum normal stress in the stress boundary layer using the extensional viscosity and extensional rate at the interface. Calculation of extensional stress based on the planar extensional rheology shows good agreement with the maximum normal stress in the stress boundary layer, indicating that given the planar extensional rheological behavior of a fluid, one can estimate the stresses that would result in the free surface displacement problem. In order to perform an accurate calculation, detailed knowledge of the flow kinematics at the interface and the wall is required. However, one can obtain good approximations for film thickness using the correlations obtained from our simulations.

For the bypass flow, the film thickness nearly scales with the maximum of the trace of the stress tensor at the tip of the bubble. The effect of shear thinning viscosity on the scaling is more pronounced because of reduced strain rates and normal stresses at the higher Ca at which the bypass flow occurs. However, as in the recirculation flow, the deviations in the collapse because of shear thinning can be accounted for by normalizing the shear viscosity with the viscosity at the wall shear rate. Furthermore, for Ca close to 1.0, the stress at the tip of the bubble can be estimated from the steady planar extensional rheology, and approximate correlations for film thickness can be determined. However, as the value of Ca becomes significantly greater than 1.0 ($Ca \approx 10.0$), we expect the transient characteristics to be important and need to be taken into account in determining the film thickness.

This work provides a comprehensive study of the effect of concentration and chain architecture of polymeric fluids on observed film thickness and normal stresses in a steady free surface displacement flow, and provides a basis for further work on understanding the effects of viscoelasticity on the interfacial dynamics of free surface displacement flows.

ACKNOWLEDGMENTS

E.S.G.S. and B.K. would like to thank NSF for supporting this work through Grants 0090428 and 0089502, respectively.

APPENDIX A: INLET CONDITIONS FOR DIFFERENT MODELS

FENE-P, Giesekus: The inlet conditions for the FENE-P and Giesekus model are more complicated due to the coupling of the out of plane components of the configurational tensor with the in-plane deformation.

For the sake of simplicity, the following abbreviations are used:

$$C_{xx} - C_{yy} = n_1, \tag{A1}$$

$$C_{zz} - C_{yy} = n_2, \tag{A2}$$

$$C_{xy} = n_3, \tag{A3}$$

$$C_{zz} = 1, \tag{A4}$$

where

$$n_1 = \frac{2n_2(1 - \alpha n_2)}{\alpha(1 - n_2)}, \tag{A5}$$

$$n_3 = \frac{(1 - n_2)^2}{1 + (1 - 2\alpha)n_2} Wi, \tag{A6}$$

$$n_2 = \frac{1 - n_4}{1 + (-2\alpha)n_4}, \tag{A7}$$

$$n_4 = \sqrt{\frac{1}{8\alpha(1 - \alpha)Wi^2} [\sqrt{1 + 16\alpha(1 - \alpha)Wi^2} - 1]}. \tag{A8}$$

Equation (A13) is introduced into Eq. (A12) for calculating n_2 , and using Eqs. (A10) and (A11), n_1 and n_3 are obtained. By setting $\alpha=0$, the inlet conditions for FENE-P are obtained.

XPP: For the XPP model it is not possible to write an analytically tractable form for $\alpha > 0$. However, it is possible to write analytical expressions for $\alpha=0$. Furthermore, since in simple steady shear flow, the rheological behavior of the XPP model is insensitive to α , we can use the inlet conditions corresponding to $\alpha=0$ for nonzero α :

$$\tau_{xx} = 3GWi \left(\frac{1}{(1 - WiS_{xy})^2} \right) \left(\frac{2Wi(\lambda_b)^2 + \left(\frac{1}{Wi} \right)}{2Wi^2(\lambda_b)^2 + 3} \right), \tag{A9}$$

$$\tau_{yy} = \tau_{zz} = 3GWi \left(\frac{1}{(1 - WiS_{xy})^2} \right) \left(\frac{1}{2Wi^2(\lambda_b)^2 + 3} \right), \tag{A10}$$

$$\tau_{xy} = 3GWi \left(\frac{1}{(1 - WiS_{xy})^2} \right) \left(\frac{1}{2Wi^2 + \frac{\lambda_b}{3}} \right), \tag{A11}$$

$$S_{xy} = \frac{Wi}{2Wi^2 + \frac{\lambda_b}{3}}. \quad (\text{A12})$$

APPENDIX B: STRAIN CALCULATIONS

In order to calculate the effective strain felt by a fluid element at the free surface in the capillary transition region where the stress boundary layer has formed, the strain rate is integrated with respect to time along the path on the free surface. Hence the effective strain can be calculated as

$$\varepsilon = \int_0^\theta \dot{\varepsilon}(t) dt. \quad (\text{B1})$$

In the case of the recirculation flow, at $t=0$ the fluid element is at the stagnation point at the interface, and at $t=\theta$ the fluid element is located at the end of the capillary transition region. For the bypass flow, at $t=0$ the fluid element is present at the tip of the bubble, and at $t=\theta$ the fluid element is located at the beginning of the capillary transition region.

Using this method of calculation, for $Ca \leq 1.0$ and for all values of $Wi > Wi_{crit}$, where Wi_{crit} is the critical Wi for onset of boundary layer formation, we determine the fluid elements to have experienced effective strains which are large enough for the steady analysis to be applicable (see Table II).

References

- Arora, K., V. Ganesan, R. Sureshkumar, and B. Khomami, "Linear dynamics of unidirectional shear flow of linear and branched polymeric melts: Eigenspectrum and stability analysis," *J. Non-Newtonian Fluid Mech.* **121**, 101–115 (2004).
- Bhatara, G., E. S. G. Shaqfeh, and B. Khomami, "Influence of viscoelasticity on the interfacial dynamics of air displacing fluid flows—A computational study," *J. Non-Newtonian Fluid Mech.* **122**, 313–332 (2004).
- Bird, R. B., R. C. Armstrong, and O. Hassager, *Dynamics of Polymeric Liquids* (Wiley, New York, 1987).
- Bird, R. B., P. J. Dotson, and N. L. Johnson, "Polymer solution rheology based on a finitely extensible bead-spring chain model," *J. Non-Newtonian Fluid Mech.* **7**, 213–235 (1980).
- Bonn, D., H. Kellay, M. Braunlich, M. Ben Amar, and J. Meunier, "Viscous fingering in complex fluids," *Physica A* **220**, 60–73 (1995).
- Bretherton, F. P., "The motion of long bubbles in tubes," *J. Fluid Mech.* **10**, 166–188 (1961).
- Brooks, A. N., and T. J. R. Hughes, "Streamline upwind-Petrov Galerkin formulations for convection dominated flows with particular emphasis on the incompressible Navier-Stokes equations," *Comput. Methods Appl. Mech. Eng.* **32**, 199–259 (1982).
- Burghardt, W. R., J. M. Li, B. Khomami, and B. Yang, "Uniaxial extensional characterization of a shear thinning fluid using axisymmetric flow birefringence," *J. Rheol.* **43**, 147–165 (1999).
- Cairncross, R. A., P. R. Schunk, T. A. Baer, R. R. Rao, and P. A. Sackinger, "A finite element method for free surface flows of incompressible fluids in three dimensions. Part I. Boundary fitted mesh motion," *Int. J. Numer. Methods Fluids* **33**, 375 (2000).
- Chilcott, M. D., and J. M. Rallison, "Creeping flow of dilute polymer solutions past cylinders and spheres," *J. Non-Newtonian Fluid Mech.* **29**, 381–432 (1988).
- Cox, B. G., "On driving a viscous fluid out of a tube," *J. Fluid Mech.* **14**, 81–96 (1962).
- Coyle, D. J., C. W. Macosko, and L. E. Scriven, "Reverse roll coating of non-Newtonian liquids," *J. Rheol.* **34**, 615–636 (1990).

- deGennes, P. G., "Reptation of a polymer chain in the presence of fixed obstacles," *J. Chem. Phys.* **55**, 572–579 (1971).
- Doi, M., and S. F. Edwards, *The Theory of Polymer Dynamics* (Oxford, New York, 1986).
- Giavedoni, M. D., and F. A. Saita, "The axisymmetric and plane cases of a gas phase steadily displacing a Newtonian liquid—A simultaneous solution of the governing equations," *Phys. Fluids* **8**, 2420–2432 (1997).
- Giesekus, H., "A simple constitutive equation for polymer fluids based on the concept of deformation-dependent tensorial mobility," *J. Non-Newtonian Fluid Mech.* **11**, 69–109 (1982).
- Grillet, A. M., A. G. Lee, and E. S. G. Shaqfeh, "Observation of ribbing instabilities in elastic fluid flows with gravity stabilization," *J. Fluid Mech.* **399**, 49–83 (1999).
- Guenette, R., and M. Fortin, "A new mixed finite element method for computing viscoelastic flows," *J. Non-Newtonian Fluid Mech.* **60**, 27–52 (1995).
- Huzyak, P. C., and K. W. Koelling, "The penetration of a long bubble through a viscoelastic fluid in a tube," *J. Non-Newtonian Fluid Mech.* **71**, 73–88 (1997).
- Larson, R. G., "Instabilities in viscoelastic flows," *Rheol. Acta* **31**, 213–234 (1992).
- Lee, A. G., E. S. G. Shaqfeh, and B. Khomami, "A study of viscoelastic free surface flows by the finite element method: Hele-Shaw and slot coating flows," *J. Non-Newtonian Fluid Mech.* **108**, 327–362 (2002).
- Lee, A. G., E. S. G. Shaqfeh, and B. Khomami, "Viscoelastic Effects on Interfacial Dynamics in Air-Fluid Displacement under Gravity Stabilization," *J. Fluid Mech.* **531**, 59–83 (2005).
- Lidner, A., D. Bonn, E. Corvera Poire', M. B. Amar, and J. Meunier, "Viscous fingering in non-Newtonian fluids," *J. Fluid Mech.* **469**, 237–256 (2002).
- Milner, S. T., and T. C. B. Mcleish, "Reptation and contour length fluctuations in melts of linear polymers," *Phys. Rev. Lett.* **81**, 725–728 (1998).
- Noda, I., Y. Yamada, and M. Nagasawa, "The rate of shear dependence of the intrinsic viscosity of monodisperse polymer," *J. Phys. Chem.* **72**, 2890–2898 (1968).
- Oene, H. V., and L. H. Cragg, "Shear dependence of reduced viscosity-concentration slope constant," *J. Polym. Sci.* **57**, 209–227 (1962).
- Park, C. W., and G. M. Homsy, "Two-phase displacement in Hele Shaw cells: theory," *J. Fluid Mech.* **139**, 291–308 (1984).
- Pasquali, M., and L. E. Scriven, "Free surface flows of polymer solutions with models based on the conformation tensor," *J. Non-Newtonian Fluid Mech.* **108**, 363–409 (2002).
- Pearson, J. R. A., "The instability of uniform viscous flow under rollers and spreaders," *J. Fluid Mech.* **7**, 481–495 (1960).
- Pitts, E., and J. Greiller, "The flow of thin films between rollers," *J. Fluid Mech.* **11**, 33–50 (1961).
- Poslinski, A. J., P. R. Oehler, and V. K. Stokes, "Isothermal gas-assisted displacement of viscoplastic liquids in tubes," *Polym. Eng. Sci.* **35**, 877–892 (1995).
- Rabaud, M., S. Michalland, and Y. Couder, "Dynamical regimes of directional viscous fingering: Spatiotemporal chaos and wave propagation," *Phys. Rev. Lett.* **64**, 184–187 (1990).
- Reinelt, D. A., and P. G. Saffman, "The penetration of a finger into a viscous fluid into a channel and tube," *SIAM (Soc. Ind. Appl. Math.) J. Sci. Stat. Comput.* **6**, 542–561 (1985).
- Ro, J. S., and G. M. Homsy, "Viscoelastic free surface flows: thin film hydrodynamics of Hele-Shaw and dip coating flows," *J. Non-Newtonian Fluid Mech.* **57**, 203–225 (1995).
- Ruschak, K. J., "Coating flows," *J. Fluid Mech.* **17**, 65–89 (1985).
- Sackinger, P. A., P. R. Schunk, and R. R. Rao, "A Newton-Rhapson pseudo-solid domain mapping technique for free and moving boundary problems: a finite element implementation," *J. Comput. Phys.* **125**, 83–103 (1996).
- Shaqfeh, E. S. G., "Purely elastic instabilities in viscoelastic flows," *Annu. Rev. Fluid Mech.* **28**, 129–185 (1995).
- Sullivan, T. M., and S. Middleman, "Roll coating in the presence of a fixed constraining boundary," *Chem. Eng. Commun.* **3**, 469–482 (1979).
- Sureshkumar, R., A. Beris, and R. Handler, "Direct numerical simulation of the turbulent channel flow of a polymer solution," *Phys. Fluids* **9**, 433–468 (1997).

- Szady, M. J., T. R. Salamon, A. W. Liu, D. E. Bornside, R. C. Armstrong, and R. A. Brown, "A new mixed finite element method for viscoelastic flows generated by differential constitutive equations," *J. Non-Newtonian Fluid Mech.* **59**, 215–243 (1995).
- Talwar, K. K., and B. Khomami, "Application of higher order finite element methods to viscoelastic flow in porous media," *J. Rheol.* **36**, 1377–1416 (1992).
- Taylor, G. I., "Deposition of a viscous fluid on the walls of a tube," *J. Fluid Mech.* **10**, 161–165 (1961).
- Verbeeten, W. M. H., G. W. M. Peters, and F. P. T. Baaijens, "Differential constitutive equations for polymer melts: The extended Pom-Pom model," *J. Rheol.* **45**, 823–843 (2001).
- Verbeeten, W. M. H., G. W. M. Peters, and F. P. T. Baaijens, "Viscoelastic analysis of complex polymer melts flows using the extended Pom-Pom model," *J. Non-Newtonian Fluid Mech.* **108**, 301–326 (2002).
- Yurun, F., and M. J. Crochet, "Higher order finite element method for steady viscoelastic flows," *J. Non-Newtonian Fluid Mech.* **57**, 283–311 (1995).